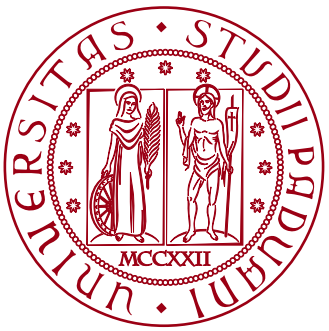

UNIVERSITÀ DEGLI STUDI DI PADOVA

Dipartimento di Fisica e Astronomia "Galileo Galilei"

Master Degree in Physics

Final Dissertation

Analysis of atmospheric pressure plasma for biological applications

Thesis supervisor
Prof. Matteo Zuin
Thesis co-supervisors
Dr. Emilio Martines
Prof. Ivo Furno

Candidate
Leonardo Zampieri

Academic Year 2020/2021

Abstract

In the last 25 years the field of plasma medicine encountered a large growth. Different sources have been developed and studied, for different purposes: among them, in the Padova laboratories the Plasma Coagulation Controller has been ideated, designed and built. The biological effects of this helium-driven source have been observed both in antibacterial applications and in blood coagulation. As for other sources, the interaction between plasmas and biological substrates which leads to observed effects is a complex combination of different phenomena and actors; the totality of the processes is still far to be understood.

Reactive oxygen and nitrogen species, generated in the interaction of plasma with atmosphere, are considered to have the main role in medical effects of plasmas: the aim of this thesis is to characterize the production of these compounds in the source, and its variation as a function of the power and environmental conditions.

The species are measured using Fourier-transform infrared absorption spectroscopy, a technique which allows a precise and fast measurement of gases concentrations. The source is therefore adapted to the optical system, providing it with all the instruments necessary to control the atmosphere in which the plasma is generated; then, all the setup is optimized, minimizing the errors and the noise sources.

As final results, the presence of ozone, nitrous oxide and nitric acid has been detected. Moreover, the variation in production of these species as function of the atmosphere humidity has been measured, proving that as the humidity rise, the production of ozone fall. Finally, the measured data are compared to theoretical models, finding compatibility.

Contents

Chapter 1

Introduction

1.1 Applications of plasmas in medicine

Plasma medicine is an extremely innovative field, emerging as a hot topic not only in the physics community but also in the medical and biological ones [Lar20; vWoe+13; Bek+19].

A plasma is an (eventually partially) ionized gas. Many different kinds of plasmas exist, in an extremely wide range of temperature and density conditions: from 10^{-5} to 10^{10}eV temperature, from 10^{-6} to $10^{24}\mathrm{m}^{-3}$ numeric density (indicative ranges), the concept of plasma collects a wide and various phenomenology. One of the main distinctions that can be done is between thermal and non-thermal plasmas. In the firsts electrons and ions are at the same temperature; there is equilibrium between the species and the plasma can sustain itself. In the seconds, instead, only electrons are hot while ions remains in a temperature close to the room one: the plasma is out of equilibrium. Being the heat capacity contribute of electrons smaller than the ions and the neutrals ones, the average temperature of non-thermal plasmas is low: therefore, they're called *cold plasmas*. The formation of a hot or a cold plasma is mainly related to the collisional properties of the system, and therefore for example to the pressure, the main ionization process, etc. This suggests that a second important distinction to consider is the pressure at which the plasma operates: for example, current main projects about nuclear fusion expect to create a plasma below 0.3Pa, and oppositely arc discharges plasmas are studied up to 1000atm. In the following, the focus will be on non-thermal plasmas operating at atmospheric pressure, namely *cold atmospheric plasmas CAPs*.

In 1996 a groundbreaking experiment regarding the killing of bacteria through cold atmospheric plasma has been published [Lar96]: the author proposes the use of an atmospheric pressure plasma to kill bacteria and disinfect contaminated matter. He describes CAPs as *unique sterilization agents*, being a combined *source of electrons, ions, excited atoms and molecules, active free radicals, and radiation (from the infrared to the ultraviolet)*. After exposing his results, he concludes the article with a set of open questions: *which plasma regime is the most effective (uniform of filamentary)? What is the minimum plasma power density sufficient to kill unwanted microorganisms? Which physical process plays the dominant sterilization role? What biological and chemical processes induce the death of the cells? Which type of gas is more desirable for a particular application?* Most of these questions still lack of a common accepted answer.

Following the successful results and the extremely innovative idea, the field of plasma medicine starts to grow and develop, involving not only physicists but also chemists, biologists and physicians. Today, biomedical applications of plasmas can be distinguished in two different approaches: the direct and the indirect ones. In the first, the biological substrate is directly treated with plasma, exposing its surface to the discharge or the downstream gas flux. In the second, instead, the interaction happens through an intermediary: a medium, which can be either water or a more complex compound as agar, is firstly treated with the plasma resulting in the so-called Plasma Activated Medium. Only in a second moment, after a time delay that can span from half an hour to more than a week, the medium is put in contact with the biological surfaces.

The field extended to treatment of both prokaryotic and eukaryotic cells, producing a wide spectrum of biologically relevant effects. Among the different applications of CAPs, one can today find:

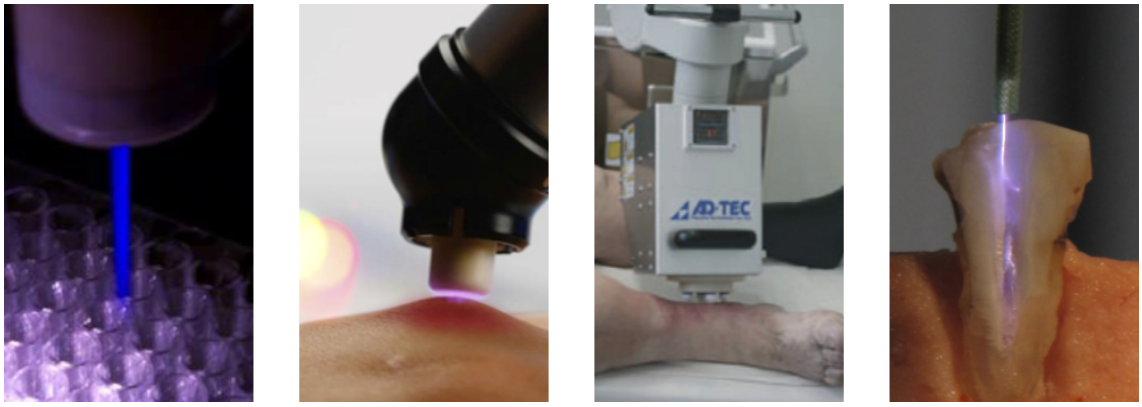

Figure 1.1: Some applications of CAPs: from left to right, plasma pencil for bacteria treatments, skin conditioning, chronic wounds healing and dentistry. Pictures from various references cited in the text.

Decontamination The inactivation and killing of microorganisms, which gave birth to the field, is still one of the most important application of CAPs. Sterilization devices which involve plasmas, typically in combination with hydrogen peroxide or UV radiation, are currently available on the market. The combined action is necessary since actual plasmas technologies are not able to act against non-cellular infection-transmitting agents, even if some studies are currently ongoing [Lar18]. Moreover, there are promising approaches for plasma-based purification of air, with the aim of removing both microorganisms and toxic pollutants [BH14].

Wound healing Both in vitro and in vivo studies have shown the efficiency of cold atmospheric plasmas in wound healing. They have been observed to enhance coagulation, to have antiseptic effects and to boost angiogenesis. Their applications span from chronic wounds to bleeding arrest in patient under anticoagulant therapies [Hae+14].

Dentistry It has been demonstrated the capability of CAPs to kill *Streptococcus mutans* and *Enterococcus fetalis*, two of the most significant microorganisms responsible for tooth decay and implant failure. With respect to the usual chemical treatments, CAPs appear to be more precise and efficient in intracanal disinfection, even if more complex to apply. Today CAPs are not only seen as an alternative to conventional treatments, but also as an opportunity of synergistic therapies. Some issues are still present: for example, the apparatus must be designed with a safety system to avoid gums burning, and the high humidity inside the oral cavity must be considered when effects are estimated. However, lots of studies are currently ongoing [GTC18].

Oncotherapy Even in treatment of cancer, CAPs show promising features: they are suitable for tumors which arise from skin or mucosal surfaces. Their ability of penetrate tissues allows to precisely target cancer cells that have infiltrated healthy ones near the tumor mass. When combined with the already in-use therapies, plasmas seem to enhance their effectivity and their selectivity: they seem to be useful both in multimodal therapies or in adjuvant ones. Lot of preclinical studies are already available, even if the theoretical basis are still being investigated [Dai+18].

A final mention must be done about the processes which use plasmas sputtering, etching, deposition and grafting abilities to optimize biological responses of various biomaterial creating intrinsically-sterile stable surfaces, suitable to be integrated with living systems.

There are certainly other applications that are here not recalled: however, still lot of work must be done, especially in trying to understand why plasmas show these behaviors and are so efficient.

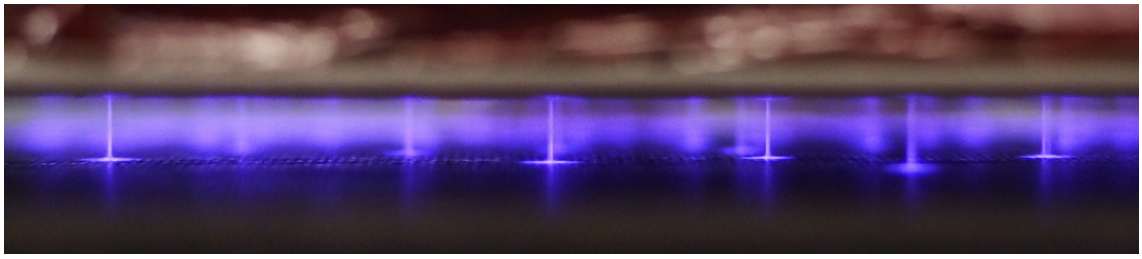

Figure 1.2: Dielectric barrier discharge between two steel plates, using mica sheets as dielectric. Depending on the characteristic of the setup, the discharge can appear more filamentous (as in this case) or more uniform. Figure from Wikimedia user Devansh.sharma, license CC-BY-SA-4.0

1.2 Generation of a cold atmospheric plasma

In biomedical applications, both the cold and the atmospheric characteristics are highly desired: one should prevent the transferring of important quantities of heat to the substrates, to avoid burning them, and should be able to operate in plain air, being biological systems not usually compatible with vacuum. With CAPs one can treat living tissue without damaging them, accessing a whole new wide set of phenomena.

The main task to achieve to obtain a plasma is to generate and heat up electrons: it is pretty usual than the generation starts from atmospheric ones (i.e. electrons normally present in every gas due to natural ionization events), which are accelerated using a strong electric field. When their energy becomes high enough they can interact with the surrounding gas and result in an avalanche effect, producing more and more electrons and rising the ionization fraction of the gas to the desired level. The voltage necessary to obtain this breakdown is influenced by different parameters: among them, gas species involved, pressure, system geometry. Moreover, the electric field used to accelerate electrons can be both stationary (continuous voltage, DC) or oscillatory (alternate voltage, AC). In DC plasmas electrons typically can reach the anode, being absorbed, which means secondary electrons production phenomena are necessary. In AC plasmas, instead, electrons oscillate between the two electrodes: if the frequency is high enough such that the electrons oscillation amplitude is smaller than the electrodes distance, they will not reach electrodes, and secondary emission effect is not necessary. The typical wideness of electrons paths, together with other plasma parameters, determines how frequent are the electron-ion collisions, and therefore if the plasma manages to reach a thermodynamic equilibrium or remains non-thermal.

One of the main issue in the design of a cold plasma source is to limit the current: being a high voltage fundamental to break the dielectric resistivity of atmospheric pressure gas, a high current can result in a high power, which means the possibility of transition to a hot voltaic arc. Moreover, in the presence of a substrate, the high power delivered can result in heating via ohmic effect, for example burning the skin. Among the different technologies available to limit the current, one can distinguish the Dielectric Barrier Discharge (*DBD*) one. The principle is to cover at least one of the electrodes with a dielectric, as glass or allumina, such that it is not in contact with the plasma. The two electrodes are then supplied with an AC voltage, typically with an amplitude of some kilovolts and a frequency in the order of kiloHertz; the electric field in the gap between the electrodes must be high enough to cause breakdown in the filling gas. The possible shapes of the discharge are various and depend on the geometry of the system: one can obtain a large set of microdischarges, or a more homogeneous glow discharge. When the electric field overcome the breakdown limit, the free electrons in the gap reach enough energy to ionize: growing electron avalanche produces a displacement current, which bridges the electrodes. But in few nanoseconds the charge accumulating on the dielectric reduces the electric field, choking the discharge and interrupting the current. Thanks to the dielectric, therefore, the peak current results to be typically less than 100mA.

Even if sinusoidal voltage were originally used to power DBDs, in the last decades it has been found that periodic short pulses offer a more efficient way to power this kind of apparatus. Nowadays, most DBDs are powered using high voltage pulses with length around ns − µs repeated

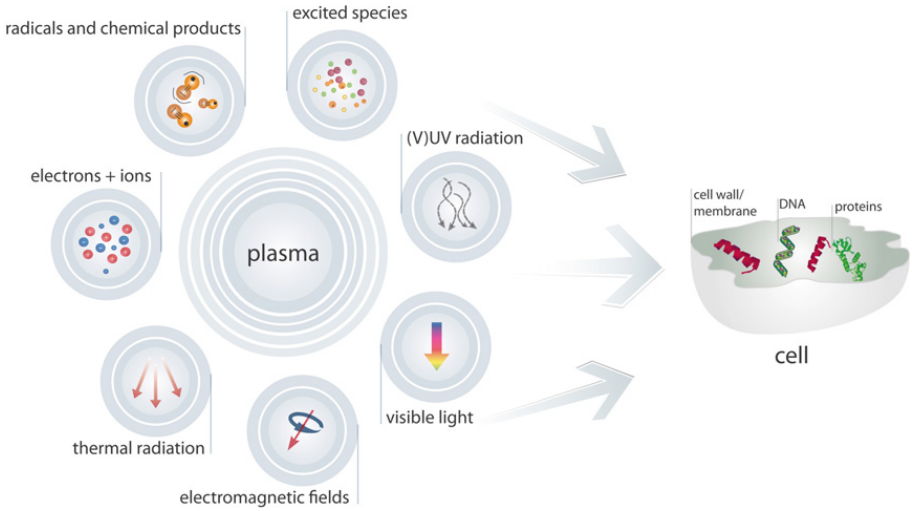

Figure 1.3: Phenomena involved in the plasma-tissue interaction. Figure from von Woedtke et al. [vWoe+13].

with kHz frequency. This setup allows to prevent both plasma thermalization, being the pulse short enough to significantly affect only electrons, and current flow, being the pulse duration shorter than the typical glow-to-arc transition time. This results in a stable, even if non-equilibrium, cold plasma.

Besides electrical details, another important parameter which distinguish DBD apparatus is the working gas: there exists sources which directly work in atmospheric air, as well as sources which work in helium, argon, neon, or mixtures of them with oxygen and nitrogen. The shape and the behavior of the discharge can clearly change for different gases.

1.3 Interaction between plasmas and biological tissues

Plasmas are complex systems and biological tissues even more; when they interact, there are many components that should be considered (fig. 1.3). Among them [vWoe+13; Kon+09; Gra14]:

Reactive oxygen and nitrogen species (RONS) When a cold plasma interact with the atmosphere or with a biological substrate, it reacts with chemicals normally present and results in the formation of various reactive compounds of oxygen and nitrogen: the DBD apparatus are usually distinguished in two classes depending on whether the dominant chemistry is the oxygen one or the nitrogen one. The formation of RONS is the consequence of photoionization and electron-particle collisions; then, they diffuse in the environment, penetrate the cells and get in contact with biological molecules. They can trigger a wide set of biochemical reactions: more than 200 reactions involving RONS and biological substrates are known. Among them, they can react with polyunsaturated fatty acids (PUFAs), forming oxidized and nitrated lipids; these, in turn, can react with proteins changing their structure or adding chemical groups, leading to the necessity of an enzymatic process to restore the functionality and to an imbalance on the correct concentration of proteins inside the cell. Also the immune system makes a strong use of RONS, and in particular they're used as messages between white blood cells; producing similar molecules, CAPs can interact with the immune system stimulating its action. As of today, RONS are considered to have the main role in the plasma medicine effects, even thanks to their central role in the *redox* chemistry.

Electrons and ions As well as RONS, even other reactive species as gas ions and electrons can have a role in the interaction with the substrate. However, their role is still not clear and no strong evidences have been found.

UV radiation Typically emitted in low concentration, UV radiation is currently under investigation for its role in plasmas-cells interactions: it is know that it can induce the production

of some vitamins, but also if in high quantity can produce strand breaks in DNA leading to tumoral forms. For example, UV radiation around 260nm can lead to a dimerization of thymine and cytosine in DNA strands, affecting base pairing and causing mutations; moreover, the cellular redox state can be disturbed by the presence of UV radiation. Typically, UV radiation is undesired in plasma source, and efforts are made to reduce it and prevent harmful effects.

Thermal radiation Most plasma source are designed for operating under 37°C, but the aim is not always fully achieved. CAP sources therefore deliver small quantities of heat, that can trigger a wide spectrum of biochemical reactions and result in burning damages.

Electric current and fields The natural resistance of dry skin is about 10kΩ: even if small, in traditional DBD devices a small current can pass through the skin, causing for example heating or triggering opening or closing of membrane channels.

Typical CAPs nowadays studied in plasma medicine have the electrons density in the range $n \approx 10^{17} - 10^{22}\mathrm{m}^{-3}$ and the electrons temperature around $T_e \approx 1 - 10\mathrm{eV}$ (i.e. $10^4 - 10^5\mathrm{K}$): a wide set of different sources is tested and used. Electrical components, feeding gases and mechanical layouts of the studied apparatus are various and the listed phenomena combine in different ways in the complete interaction. This lead to the difficulty in comparing results: being the interaction so complex, it is hard to define a quantification standard, an equivalent to the radiation *dose*. Following this issue, there are no comparative studies about the efficiency of biomedical plasma sources, and it is not trivial the meaning of *optimizing* a prototype.

1.4 Biological behaviors

Following the interaction of CAPs with biological tissues, chains of biochemical events can be triggered leading to more complex phenomena: among them, the oxidative stress or the wound healing processes.

1.4.1 Oxidative stress

Oxygen is well known to be an important component in the biochemical processes which sustain the life of a cell. In particular, its high reactivity allows participating in the transfer of high-energy electrons and therefore in the formation of adenosine triphosphate (ATP) via oxidative phosphorylation. If, on one hand, the reactivity of oxygen is fundamental for the cell to survive, on the other hand makes it eligible to react with virtually any other molecule. From a certain point of view, one can state that a cell is constantly under the attack of oxygen reactive species (ROS): to prevent serious damages, a wide set of antioxidant mechanisms has developed to keep the proper balance, called *redox equilibrium* [BJ11].

External factors, however, can affect the concentration of ROS inside the cell: occasionally, if the change is significant and the antioxidant mechanism does not manage to counteract it effectively, perturbations in the correct balance can emerge, leading to the so-called *oxidative stress*. Clearly, the boundary between normal physiological oscillations of oxidant-antioxidant ratio and stress condition is indistinct. Similarly, the response of the cell is graded: from a homeostatic adaption for small imbalances, to several damages and apoptosis in severe cases.

Among the principal RONS involved in redox equilibrium one must cite the superoxide anion O_2^-, mainly generated by leakages in mitochondria respiratory chain, and its first enzymatic product, hydrogen peroxide H_2O_2. The first is more reactive and therefore dangerous, but its ionic character prevent him to diffuse through membranes, keeping it typically trapped inside mitochondria; the second, instead, even if less reactive, is non-polar and therefore able to diffuse in the whole cell. Fundamental to counteract the effect of hydrogen peroxide is the catalase enzyme, which detoxify it to water.

On the other side, both enzymatic and non-enzymatic defenses can prevent this kind of stress. Detoxificant enzymes are typically characterized by a metal, responsible for the electron transfer: among them the superoxide dismutase, in the manganese isoform or in the copper-zinc one,

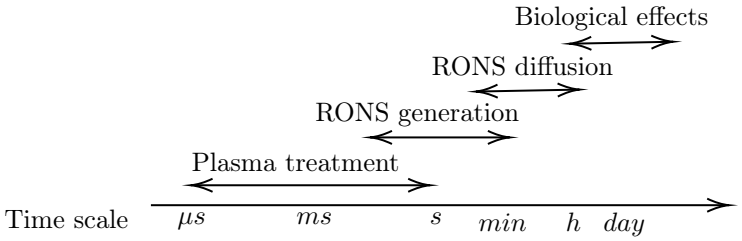

Figure 1.4: Typical (indicative) timescale of plasma treatments. Inspired by Keidar [Kei18].

responsible for O_2^- breaking in H_2O_2, and the already-cited catalase, with its iron core. Regarding non-enzymatic defenses, these include vitamins C and E and thiol compounds, capable of detoxifying RONS.

Among the effects of oxidative stress on cell functions, one must consider the activation of redox-sensitive transcription factors. Some of them regulates cell signaling, differentiation and apoptosis. For example, the factor NF-$\varkappa$B is inactive under normal conditions; however, oxidative stress can affect the inhibition sub-unit and activate the factor, which means producing pro-inflammatory signaling molecules and, if the yield is high, activate the apoptotic cascade. Moreover, proteins can be modified and made ineffective: for example protein kinases, a particular class of enzymes responsible for proteins phosphorylation, can be over-activated by the presence of ROS. Even if in extreme conditions these effects can lead to apoptosis, they are still considered physiological adaptive changes.

More severe ROS attack may lead to a wider set of responses, through more pathological effects. High imbalances of ROS are able to activate calcium release channels in the endoplasmic reticulum, disturbing the equilibrium of Ca^{2+}-sensitive processes, which include most of the signalling pathways, and adversely affect mitochondrial functioning. Moreover, hydroxyl radicals are capable of causing lipid peroxidation, destroying the membrane of organelle, and oxidation of amino acids, leading to detrimental proteins modifications. Finally, ROS can attack even DNA, and in particular mitochondrial DNA, causing strand breakages, mutations and aberrant gene expressions.

When a living cell is treated with a cold atmospheric plasma, the RONS generated can manage to permeate the cell and cross the membrane: reaching the cytoplasm, they can affect the redox equilibrium of the cell leading, with the exposed mechanisms, to oxidative stress. The timescale of the mechanisms is reported in fig. 1.4: apoptosis can happen even after days from the treatment.

The *oxidative stress* is the same mechanism which allow plasma oncotherapy. While in normal cells the levels of RONS are well below the oxidative stress threshold, in the mutated cancer cells they are typically raised to enhance the reproduction mechanism, and therefore only slightly below the threshold. When a plasma get in contact with some cells, if slightly rising the RONS level for healthy cells is not a problem, for tumoral ones this small imbalance can lead to reaching the exposed pathological effects. Moreover, it has been observed that cancer cells tend to have a larger number of H_2O_2-permeable channels (aquaporins) on their membrane, allowing a selective infiltration of the compound, and at the same time a lower availability of catalase. When the external environment shows an anomalous concentration of hydrogen peroxide, therefore, it will tend to enter the cancer cells and accumulate inside, breaking the redox imbalance and, through oxidative stress, leading to apoptosis. Promising results have been obtained regarding even *in vivo* treatments of glioblastoma using CAPs [Kei18].

1.4.2 Wound healing

Plasma has been observed also to trigger blood coagulation processes: however, the mechanism is really complex and, as today, still not fully clear. Performing a set of experiments, lots of factors have been excluded from the mechanism responsible for the plasma-assisted blood coagulation. For example, covering the blood sample with a thermal-conductive lid the coagulation effect has been observed to disappear, suggesting that the triggered process is not thermal-induced.

The natural blood coagulation process is complex but extensively studied: a simplified scheme

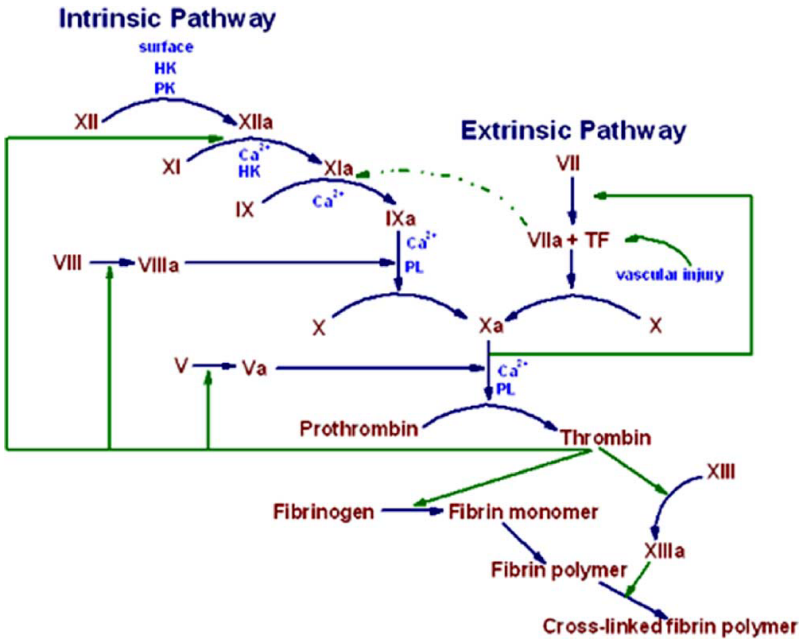

Figure 1.5: Simplified coagulation cascade. Figure from Kalghatgi et al. [Kal+07].

of the biochemical cascade is reported in fig. 1.5. It is immediate to recognize the important role of Ca^{2+} in the cascade: one of the first hypothesis on the role of plasma was to increase Ca^{2+} concentration through a redox mechanism. However, some measurements have proven that its concentration does not vary significantly during treatment. Similar measurements show that electric field, light, temperature and change of blood pH are not responsible for blood coagulation triggering.

As shown in fig. 1.5, the conversion of fibrinogen in cross-linked fibrin fibers is one of the final steps the coagulation cascade: one of the most accredited hypothesis states that plasma treatments directly affect fibrinogen, and in particular converting it to larger molecular structures. After plasma treatments, in fact, it has been observed the appearing of fibrinogen clusters with an average size of 2µm (the typical size of a fibrinogen molecule is around 9nm) which facilitate the subsequent conversion to fibrin fibers. The physical-chemical mechanism that induce this aggregation is still not clear and being studied [Kal+07].

Some other studies, instead, seem to point out a completely new mechanism stimulated by plasma which lead to blood coagulation. In particular, it has been observed aggregation of proteins like albumin or immunoglobulin G, typically dissolved in blood serum and not commonly involved in blood coagulation processes: the coagulated material therefore appears to be slightly different in shape from the natural one [Ike+15].

The exact mechanisms for both coagulation paths, however, still have to be completely understood yet.

Besides the coagulation of blood, other biological activities are involved in wound healing: for example, the activation of immune system for the recognition of pathogenic organisms. This is manifested by inflammation, whose function includes cleaning the injury and initiate tissue repair. RONS have a key role in the activation of the innate immune system, both on promoting and resolving inflammation; in particular in signaling, amplification and anti-pathogen cytotoxicity. At the same time, an excessive presence of RONS can prevent the correct termination of the immune response and lead to chronic inflammation which causes pathological damages [Gra12].

Nitric oxide NO is thought to be the most important species when speaking about wound healing. It acts not only on the coagulation chain, but also in angiogenesis and matrix deposition. With the aim of improving and speed up coagulation, studies about the use of NO sources, both external (like plasma sources but also more specific apparatus) and internal (like gene therapies for the enhancement of NO-creating enzymes), are currently active.

Lots of different effects can be listed, some of them still to be fully understood. A recent work, for example, states the existence of a totally new cell death type, characterize by a rapid leakage of cytosol in bubbles from the cell membrane and consequently in a shrinkage of the cell. This particular effect has been observed to be independent of RONS presence, and in particular to happen even if between the plasma and the biological substrate a glass barrier is placed [Yan+20].

The combination of physical and chemical components, together with the complexity of biological reaction chains, does not allow carrying out a complete theoretical study of the plasma-tissues interaction. Today, lots of works are ongoing to try to correlate the biological effects with the physical properties of the source; however, new effects are continuously discovered, and still lot of work is needed to fully understand the involved processes.

1.5 Outline of the thesis

This thesis work is devoted to study and characterize a particular plasma source, called Plasma Coagulation Controller PCC, which has been developed in Consorzio RFX laboratories, in the Padova area of the National Research Council. The source has been observed to be able to produce interesting biological effects, like disinfection and blood coagulation; however, its characteristics in terms of reactive oxygen and nitrogen species production are still unknown. The aim of this work is therefore to detect the production of RONS from the source, trying to understand which species are mainly obtained; secondly, dependence of chemicals production from the environmental conditions in which the source operate is to be studied. The main diagnostic chosen to pursue the objective is the Fourier transform infrared spectroscopy.

The report is structured as following:

CHAPTER 2 describes the source, its principle and its electrical behavior. Then, a brief recap of the results from previous studies on the biological effects of the PCC is reported;

CHAPTER 3 focus on the Fourier transform infrared spectroscopy apparatus and the experimental setup: starting from the theoretical basis, the integration of the source with the spectrometer is exposed;

CHAPTER 4 report the first spectroscopic measurements, and focus on spotting the main issues. Then, an improvement of the setup is carried out, optimizing the system to enhance the sensibility and reduce the noise, managing to detect the main produced RONS;

CHAPTER 5 finally introduce the parameters of distance from the nozzle and of humidity, studying how the chemicals production changes along the plume and in different humidity conditions. In particular, the interesting behavior of ozone production is measured and successfully compared with physical and chemicals theoretical models.

Finally, the obtained results are summarized, highlighting the most interesting points and exposing the relevance of the obtained data; to conclude, some further work proposal are stated.

Chapter 2

The source: Plasma Coagulation Controller

In the laboratories of Padova section of *Consiglio Nazionale delle Ricerche CNR*, and in particular in the RFX consortium, a program on plasma applications for medical purpose is currently ongoing. The team worked on some sources with different layouts, with the aim of optimize the physical structure to maximize the biological effects. Between the realized sources, the Plasma Coagulation Controller (PCC) is one of the last projects, based on the principle of a pulsed DBD [Cor+19a; De +18; Man19].

2.1 Main structure

The source itself consist in two bodies: a power supply (fig. 2.1(a)) and the proper source body (fig. 2.1(b)). The source is designed to be totally user-friendly: the body is light and handy, thought to be easily used by a medical operator. From outside, it appears as a 3D-printed plastic cylinder of total length about 20cm and diameter around 50mm. It is connected to the power supply, a black box provided with a display and a set of buttons which allow the working parameters to be easily controlled. Moreover, a gas pipe must be connected to the source, with a flow meter to properly regulate the gas flow.

Inside the power supply, which can be simply connected to the domestic electrical network, are hosted the electrical transformers and the control system. An Arduino Leonardo microcontroller remotely controls the discharge: a graphical interface and a set of buttons allow both to use a predefined set of parameters or to manually set choose them. The case is connected to the body with a couple of copper wires, which leads a constant 22V DC power supply, and an optical fiber,

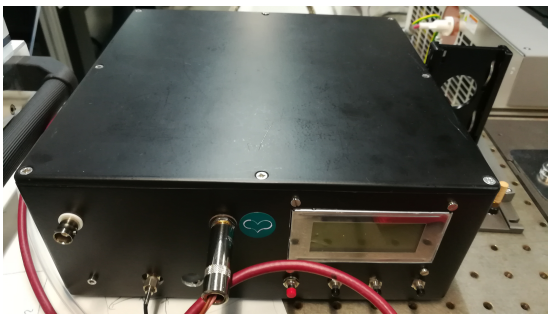

(a) The power supply

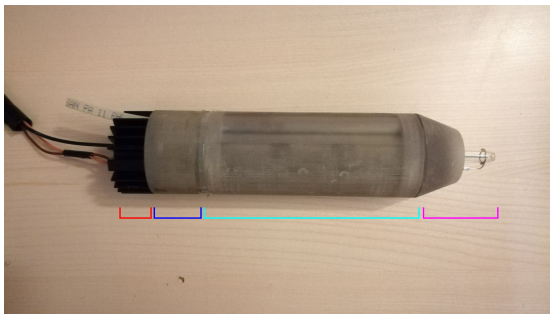

(b) The external body. The main sections can be spot: heatsink (red), circuit (blue), transformer (cyan), nozzle (magenta)

Figure 2.1: The Plasma Coagulation Controller

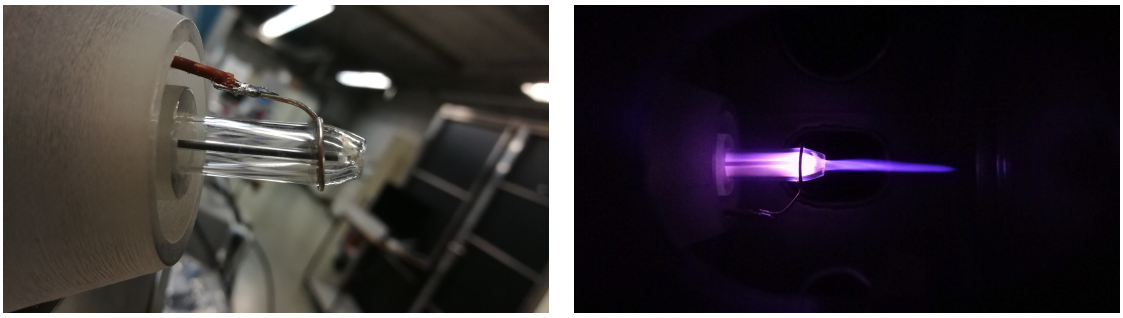

(a) The nozzle: the internal electrode is clearly visible, and it is covered with a thin Pyrex capillary. Externally, a larger Pyrex nozzle contain the gas flux. Also, the ground ring can be seen.

(b) The discharge. Both the internal electrode and the external ground ring are visible.

Figure 2.2: The tip of the PCC, and the plasma plume formation.

which transmits the signal for the charging and discharging of the source. The transmission of the trigger signal via an optical fiber allows to prevent that possible reflections from the high voltage discharges on the body can return back to the case, damaging the control system. The two parts of the PCC are therefore electrically uncoupled, if not for the shared power supply.

In the source, instead, four different sections can be recognized (fig. 2.1(b)). On the back of the source, where the electrical cables, the optical fiber and the gas pipe are connected, a metallic heat sink prevents the circuit from overheating. The first part of the body is where the circuit for the generation of the high voltage discharge is hosted. The main components of the circuit are a silicon PIN photodiode and a power MOSFET: the first reads the control signal from the optical fiber, and it is connected to the gate of the second, controlling the opening of the channel. A power driver and a system of resistors and capacitors ensure all the components the proper power supply, as well as an adequate protection from the discharge feedbacks. In the central, and larger, section of the source body a three-coils transformer with ferrite cores is hosted. The MOSFET controls the passage of current in the primary winding; the secondary is connected to the nozzle electrodes. When the optical signal lights up, the photodiode activates the MOSFET channel: a current starts to slowly rise, limited by the coil inductance, in the primary winding of the transformer. When the optical signal switches off, the photodiode suddenly stops the MOSFET conductivity: the current in the coil is sharply interrupted, resulting in a big variation of the magnetic flux in the transformer cores and therefore inducing a large potential difference in the secondary winding. The voltage obtained is clearly function of the current reached in the primary winding before the interruption, and therefore of the opening time of the MOSFET: using optical signals with duration around some micro-seconds, the electrode is able to reach voltages in the order of some kilovolts. The pulse produced this way is homopolar, since only the current interruption is sharp enough while the current rising is smoother, and synchronized with the falling edge of the trigger signal. With a sequence of regular optical signals, a sequence of discharges can be triggered: the range of frequencies available in the control module is between 1 and 20kHz.

The last section of the source is where the dielectric barrier discharge physically take place: it consists in a central graphite electrode covered with a Pyrex capillary, and in a Pyrex nozzle. The latter has a 6mm internal diameter and in the final part it shrinks to 3mm internal diameter. Both the capillary and the nozzle have the role, as planned by the DBD concept, to interrupt the discharge and prevent high currents. Using a dedicated pipe, which enter the source from its back and pass through all its body reaching the tip, between the capillary and the nozzle a gas is flown: helium, neon or argon can be all used for powering the source, with typical flow of $1 - 4$L/min. In this work, only helium is used as working gas. Eventually, a ground metallic ring can be placed outside the nozzle: depending on the used gas and its properties, the discharge can efficiency happen also without the ring. Particular attention is paid to the sealing of the system: it is important to lead all the injected gas to the nozzle. If some leaks or an uncontrolled diffusion lead some gas to the transformer or the circuit, discharges can happen inside the source body

causing a burn out of the electrical components.

When the source is switched on, a plume is formed: a bright jet which can reach the length of 10cm (fig. 2.2(b)). The size and the shape of the plume depend on the parameters of the discharge, while the color is due to the feeding gas and the interacting atmosphere. The plume is a cold atmospheric plasma: it can be touched even for some minutes without feeling heat on the skin. Thanks to the shape of the nozzle and the attention paid to the sealing of the gas system, a proper outflow is guaranteed independently of the orientation of the source: it can be moved, rotated, faced up or down and the plume still correctly generates in the direction of the nozzle.

Previous studies, and in particular images of the plume with fast cameras and chemical simulations, showed that the jet is not uniform as it can normally seem. Instead, it consists in a series of streamer discharges, which rapidly propagate following the helium flux with a speed way higher than the gas one. It is only thanks to the high frequency of the discharges, and therefore to the production of thousands of bullets per second, that the plume appears continuous. The shape and the speed of the bullets depend on the chosen gas and the discharge parameters, but in general their velocities are measured to be between 10 and 150km/s.

The phenomenon of bullet formation and propagation, observed in different plasma jet apparatus, still has to be totally explained; significant efforts have been made to develop theoretical models which fully explain experimental observations. Most of the available theories recognize the importance of the helium-air diffusional mixing layer as a medium which guide and sustain the propagation of the streamer: it has been recognized that the concentration of electrons and RONS reach a maximum not along the axis of the plume but in the layer where the air molar fraction is about 1%. This means that if the source is operated in vacuum or in a saturated helium atmosphere the plume cannot properly develop: most of the models state that an atmosphere with breakdown threshold higher than the discharge gas is fundamental for the streamer propagation [BMR12; JLK10].

The streamer is sustained by the high electric fields, which drive electrons-impact reactions; some theories states that the formation of plasma bullets and their propagation in the tube is related to the ionized helium atoms which accumulate and spread on the dielectric surface near the electrodes. When a sufficient amount of positive ions accumulates on the dielectric surface, they generate an electric field which is able to ionize other helium atoms, producing an ionizing wave which propagate along the tube. When the ionization front reach the mixing region, oxygen and nitrogen enter the helium channel leading to a modification of the propagation mechanism: the bullets seems to behave like propagating streamers, with a positive space charge generating high electric fields. Besides photo-ionization mechanisms, which generates new electrons in front of the bullet, electron-avalanches can trigger electron-particle collisions, involving nitrogen and oxygen and leading to the formation of RONS. Among them, the formation of nitrogen excited states, which allows the propagation of the streamer:*:

$$e^- + N_2 \longrightarrow N_2^+ + 2\,e^-$$

together with other excitation processes, like the charge transfer:

$$He_2^+ + N_2 \longrightarrow 2\,He + N_2^+$$

and the Penning effect:

$$He + He + N_2 \longrightarrow 2\,He + N_2^+ + e^-$$

The combination of all these processes allows to keep a high availability of energetic electrons and for the streamer to propagate.

Observing fig. 2.2(b), one can identify in the white glow inside the nozzle the effective helium plasma; instead, in the purple plume exiting the nozzle one can recognize the propagating streamers of mixed helium-air plasma, whose color is given also by nitrogen and oxygen ionization lines.

*For a complete description of these reactions, which specify the excitation states of each molecule, see [JLK10]

2.2 Electrical behavior

The signal which travels in the optical fiber can be assumed to be a digital one: the LED can be either on or off. The state of the LED is therefore modelled with a square wave, which have two parameters controlling its shape: the frequency of the pulses and the length of each pulse. These two parameters, remembering the role of the photodiode inside the source body, control two properties of the discharge: while the former directly controls the frequency of the discharge, the second (called *opening time*) is related to the charging time of the transformation circuit, and therefore indirectly related to the voltage amplitude of the discharge.

The system, using the interface on the power supply, allows setting up both the parameters: the frequency in the range between 1 and 20kHz with a 1kHz resolution, and the opening time in the range between 1 and 8µs with a 1µs resolution. In this work, basing on the previous biomedical studies and to keep a uniformity in the results, three predefined working regimes have been considered. They're defined as following:

Low power Frequency 5kHz, opening time 2µs;

Mid power Frequency 2kHz, opening time 4µs;

High power Frequency 10kHz, opening time 4µs;

Let's observe that the first one have a shorter opening time, and therefore is expected to generate a lower potential difference for the discharge; the second and the third one have the same opening time, and therefore almost the same voltage, but different frequencies.

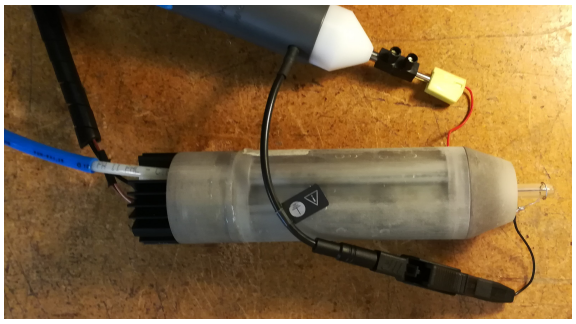

Figure 2.3: The probe connected to the PCC. The red cable is internally welded to the base of the graphite electrode; the black one, instead, is welded to the ground ring.

To properly characterize these three regimes, the discharge voltage has been measured. The source has been disassembled to be able to reach the base of the graphite central electrode; there, a small cable is welded and conducted outside the source, which is then reassembled (fig. 2.3). Another cable, instead, is externally welded to the ground ring. A high voltage probe, PHV4002-3 from hivolt.de, has been chosen: it allows measuring pulses up to 40kV and with a bandwidth of 100MHz, applying an attenuation ratio of $1 : 1000$. The probe is connected to the source using the just welded cables, and the detected voltage is measured using a Teledyne Lecroy HD4096 oscilloscope.

To carry out complete measurements, the power supply has been slightly modified. The signal produced from the arduino and controlling the LED is doubled, and the free extremity is decoupled using a logical gate and a low-pass RC filter. The output of the gate is, using a BNC connector, made available from the front panel of the case: in this way a trigger, exactly reproducing the optical fiber signal, can be acquired.

The oscilloscope is set to trigger on the falling edge of the just-installed signal of the power supply, and to measure the voltage from the source electrode averaging over 1000 samples. The results (without helium flow) are reported in fig. 2.4, in which both the pilot signal and the resulting pulse in the electrode are shown. As can be observed, the opening time lasts 2µs for the low power regime and 4µs for both the mid and the high power one, as expected. When the pilot

signal falls down, after a small delay, all the energy loaded from the ferrite cores is released in a fast voltage shot. The shot is homopolar: the electrode reach a positive potential of some kilovolts. After the shot, a set of oscillations relaxes the system. Also the effect of the signal reflections can be observed: in correspondence of the high voltage peak, a small noise is visible in the trigger signal. It can be ascribed to the reflections on the source circuit of the high voltage discharge, which go back in the main case through the power supply cables and disturb the transformer. However, thanks to the use of the optical fiber to carry the signal and the presence of low-passing filters, the noise is quite low.

Enhancing the horizontal resolution to better observe the peaks, the measurements are repeated both without helium flow and with a 2L/min helium flow through the source, which means without and with the discharge and the plume. The results are reported in fig. 2.5.

From the plot the shape of the voltage peaks, their width and their height are clearly visible, and can be measured to define the properties of the discharge. In particular, one can define the peak height, computed using a quadratic interpolation on the top of each signal, and the full width at half maximum (FWHM), representing the time interval in which the voltage overcome half of its maximum value. The measurements are repeated multiple times in all the conditions, averaging the results and defining the errors (the instrumental errors from the probe and the oscilloscope are negligible with respect to the errors from the averages). In table 2.1 the estimated values are reported.

Power	Discharge	Peak [kV]	FWHM [µs]
Low	No	5.1 ± 0.1	0.41 ± 0.03
	Yes	4.8 ± 0.1	0.41 ± 0.03
Mid	No	7.7 ± 0.1	0.43 ± 0.03
	Yes	7.1 ± 0.1	0.45 ± 0.03
High	No	7.2 ± 0.1	0.43 ± 0.03
	Yes	6.7 ± 0.1	0.45 ± 0.03

Table 2.1: Results from the voltage peak measurements. Errors are obtained through multiple measurements.

In particular, one can observe that:

- the Full With at Half Maximum of the voltage peak is, as a first approximation, constant over the three regimes and can be estimated around 0.43 ± 0.3µs;
- the voltage peak is around 5kV for the low power regime and around 7.5kV for the medium and high power regime. As expected, the voltage magnitude is mainly dependent from the opening time;
- a small dependence of the voltage peak from the frequency is observed: in the high power regime the peak is about 0.5kV smaller than in the mid power one. This difference can be ascribed to a loss of efficiency of the MOSFET inside the PCC circuit due to the short relaxing time available;
- in presence of helium, and therefore when the plume is formed, the peak voltage is slightly smaller.

The results are in agreement with the ones reported in Mancini [Man19].

2.3 Biological effects

The interest in the study of the source is mainly due to the biological effects of the source, and therefore to its medical applications. In particular, in a previous work the interactions with bacteria or with blood have been studied [De +18].

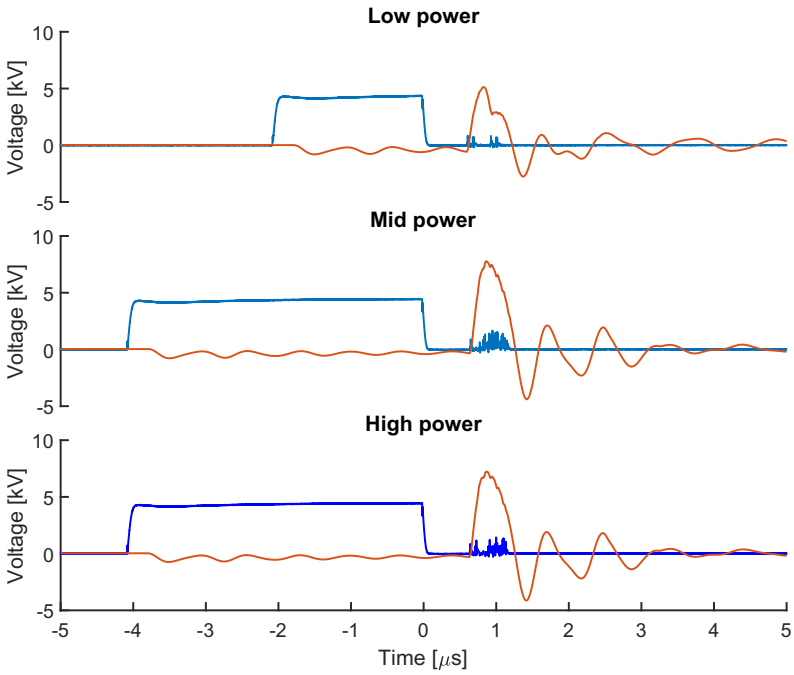

Figure 2.4: Trigger signal (blue) and voltage at the electrode without the helium flow (orange), for the three power configurations. The trigger signals have been properly rescaled to make them visible.

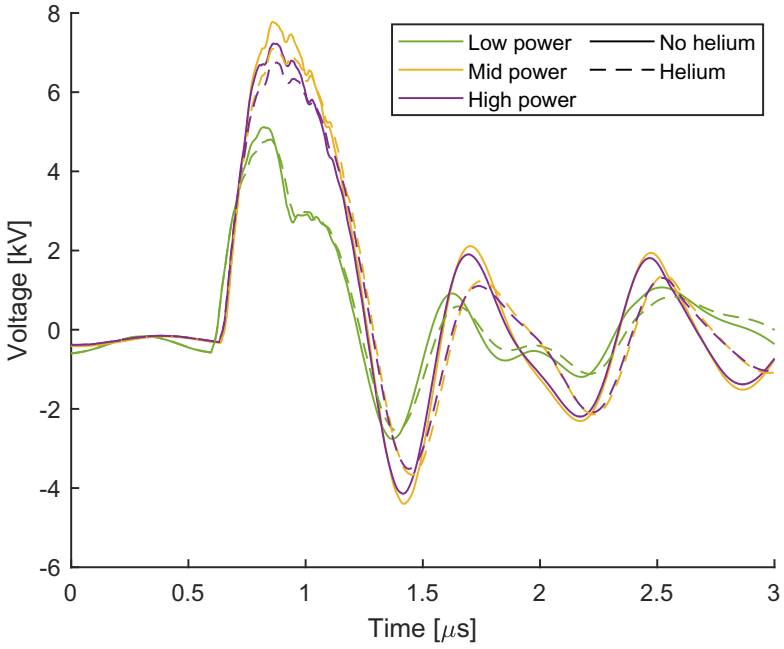

Figure 2.5: Signal with and without the helium flow: focus on the discharge interval.

Antibacterial effects

The PCC has been tested both with Gram-positive and Gram-negative bacteria strains: *Escherichia coli*, *Staphylococcus aureus* and *Pseudomonas aeruginosa*. Bacteria are firstly grown in a proper medium, and then the cultures are diluted, incubated and shaken. After a series of dilutions leading to an adequate colony-forming unit (CFU) density, they are placed in culture plates. They are then exposed to the PCC helium plume, for different time intervals between 15 and 120s; for the reported measurements, the treatment is done in the middle power configuration. After exposition, bacteria are left to grow and their vitality is evaluated as a ratio in the CFU between the treated and the untreated samples. Results are reported in fig. 2.6.

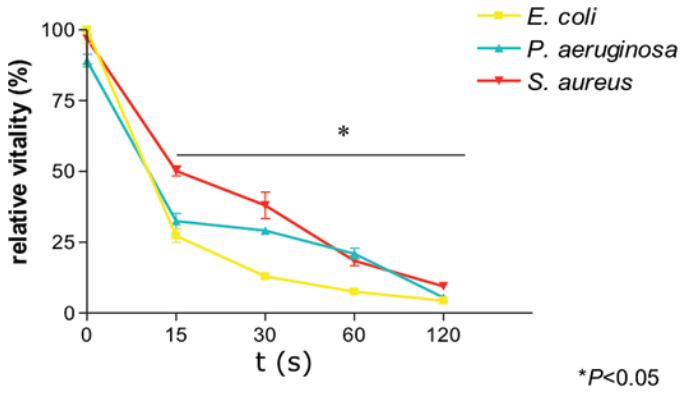

Figure 2.6: Vitality ratio of three different species of bacteria, as function of PCC treatment time. Plot from De Masi et al. [De +18].

As suggested by the plot, for all the three species the PCC results to be very efficient as a bactericide. After only 15s of treatment the relative vitality drop to less than 50%; moreover, it keeps decreasing as the exposition time increase almost reaching the complete disinfection after 2min.

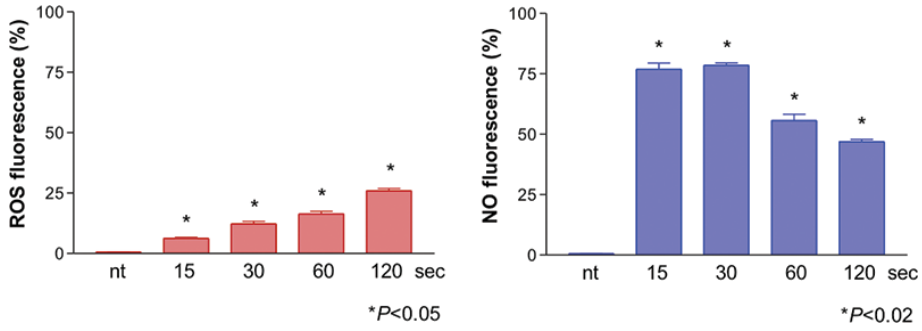

Figure 2.7: Presence of ROS in human fibroblasts cells, in percentage of cells positive to fluorescent dye; *nt* label the non-treated sample. Plots from De Masi et al. [De +18].

Remembering the aim of this thesis work, which is to study the production of RONS in the plume, the studies carried out on human fibroblasts cells are of particular interest. The cells are drugged with proper dyes which highlight the presence of reactive oxygen species and of NO; then, they're exposed to the helium plume for different treatment times, always using the middle power configuration. Finally, the cells are sorted using fluorescent-activated cell sorting analysis. The results are reported in fig. 2.7, in which the percentage of human fibroblast cells turned out to be positive to the dye fluorescence is plotted. As can be observed, the presence of RONS is highly enhanced by the treatment; in particular, ROS shows the expected behavior rising proportionally to the exposure time. A bit more complex is the process involving NO, which suddenly rises when the treatment starts and then slowly decays. The detailed cellular mechanism still need investigations, but there is a clear suggestion that PCC action has a link with intracellular RONS.

During this thesis work a rough observation of the bactericide effects has been carried out, as a collateral test to verify the functionality of the source. A set of solutions of *Escherichia Coli* has been prepared, in which each sample is 10 times more diluted than the previous one. The bacteria solutions are then spread on Petri dishes, previously covered with an appropriate growth medium. All the dishes are treated with the PCC, in their center using the high power configuration for 3min and with the nozzle at about 2cm from the medium surface. Finally, the dishes are left for 24h in an incubator. The results are reported in fig. 2.8.

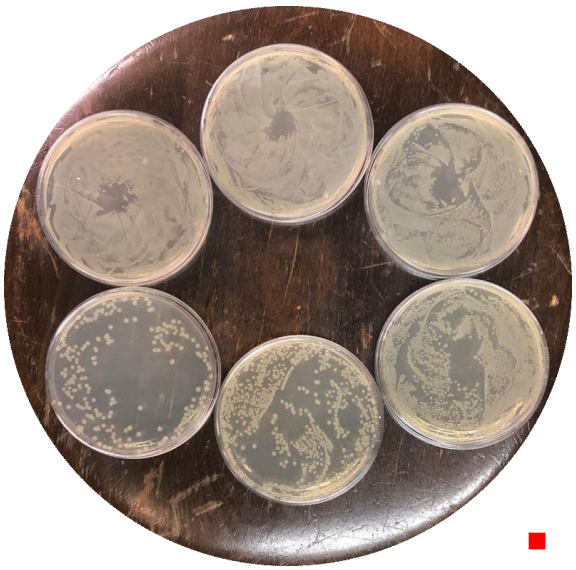

Figure 2.8: Bacteria colonies after 24h. Starting from the upper left dish and proceeding clockwise, each dish was initially populated with a bacteria concentration 10 times lower than the previous one. At the center of each dish can be clearly observed the treatment area, showing a total extinction of colony forming units. The red marker, for scaling reference, is a squared centimeter.

In each dish, from the most diluted one with countable colony forming unit to the most concentrated one with an almost uniform layer of bacteria, the central spot where the treatment has been performed is clearly visible as a total absence of colonies in an area with a couple of centimeters of diameter. Even if the study is very preliminary, the PCC bactericide effect results to be very powerful: it guarantees a complete reproductive death of *Escherichia Coli* for all the concentrations considered; at the same time, however, the effect seems to be very localized around the plume.

Blood coagulation

In the same work previously cited also blood coagulation *in vitro* studies are reported. Blood samples are withdrawn from patients under anticoagulant therapy, and therefore are expected not to coagulate spontaneously. 200µL samples are prepared and transferred on plates and treated for different times at different power levels. 24h after the treatments, the presence of blood clots has been evaluated (fig. 2.9).

For all the source parameters, a significant (ANOVA: $p < 0.01$) difference between the treated samples and the control one has been found; it can be stated that the PCC treatments significantly enhance blood coagulation. Given the small amount of samples and the large variance, the authors were not able to observe significant differences between the various parameters configurations.

In another work from the same authors, histological analysis of the coagulation phenomena has been performed. Using again blood samples from patients undergoing anti-coagulant therapy, 50µL blood drops has been placed on a glass slide and treated with the PCC at 1cm of distance, using different treatment time and powers. After about 1h of drying in air, the strains have been fixed and observed [Cor+19b].

The histological analysis (fig. 2.10) has shown both platelets aggregation and fibrin polymer-

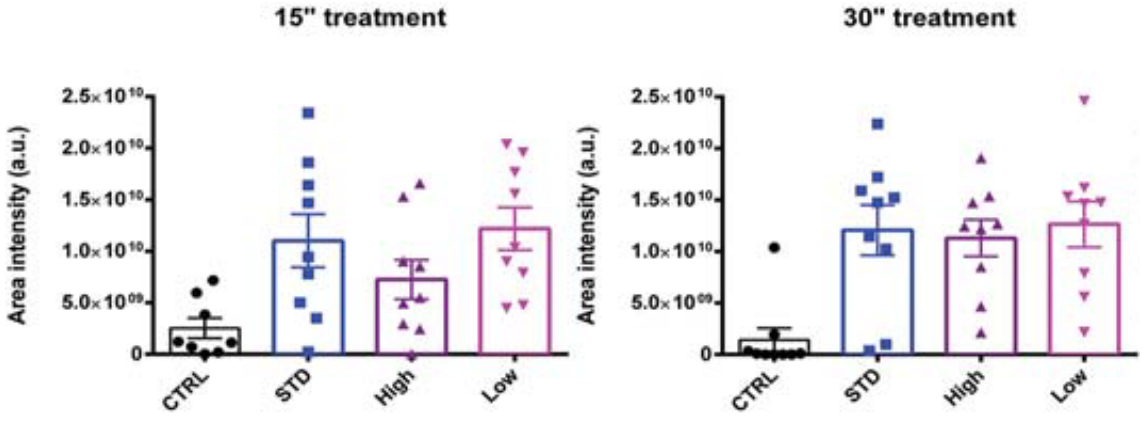

Figure 2.9: Coagulation area intensity 24h after the plasma treatment in the blood samples, for different power level (*CTRL* label the non-treated sample, *STD* the mid power) and treatment time. Plots from De Masi et al. [De +18].

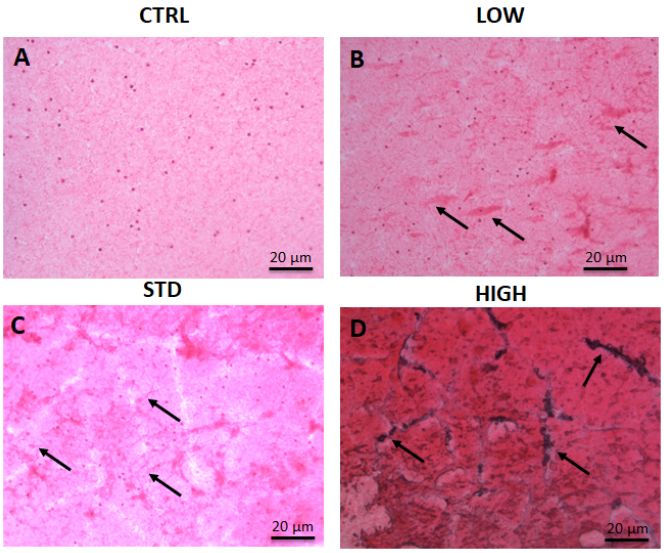

Figure 2.10: Histological analysis of coagulated blood: representative images after 60s treatment. The arrows indicate some platelet aggregates and fibrin networks (*CTRL* label the non treated sample, *STD* the mid power). Figure from Cordaro et al. [Cor+19b].

ization, with a percentage of aggregation proportional to the treatment intensity. However for high intensity an adverse effect appears: besides the extreme platelet aggregation and fibrin polymerization, also a robust red cells lysis is observed. In the high-treated sample, moreover, some black colored spot are visible in correspondence of platelet clot areas, possibly due to accumulation of iron released from broken red cells.

The results in terms of electrical behavior, plume development and biological effects suggest that the PCC produces a significant amount of reactive oxygen and nitrogen species; however, direct measurements have never been performed. The knowledge of the produced RONS, and their sensitivity to the control parameters and the environmental conditions, can help not only in optimizing the source and defining the best treatment protocols, but also in understanding the biochemical chains behind the observed effects.

Chapter 3

The diagnostic: Fourier-transform infrared spectroscopy

The technique chosen to measure the presence of RONS is the Fourier-transform infrared spectroscopy, using an *in-situ* layout: the measure is performed directly on the plume. The system allows detecting small quantities of gases but must be adapted to install the source. In the following, the bases of the technique are exposed and the experimental setup is described.

3.1 Spectroscopy in the infrared region

As *infrared spectroscopy* is named a set of methods and techniques which aim to measure emission or absorbance spectrum of a sample in the infrared spectrum, which means for electromagnetic radiation in the wavelength range between 700nm and 1mm. These techniques have a wide application range, allowing to study structures of molecules from small ones to complex ones. Recently, it has been also used to mapping cellular components and applied to the study of proteins [BH09].

Functional groups, which made up molecules, can be associated with a set of fundamental vibrations of the chemical bonds: given a non-linear molecule with N atoms there are $3N - 6$ fundamental modes of vibration. Each one is electromagnetic active if it corresponds to a variation on the dipole moment of the molecule; in particular, they are typically active in the infrared region of the spectrum. For groups with a permanent dipole, larger absorptions are usually observed.

Functional groups vibrations can be identified in two types: stretching vibrations, which are related to the distance between couples of bonded atoms and therefore to the length of bonds, and bending vibrations, which concern the angles between bonds. The first ones can be easily modelled using a harmonic oscillator, and therefore their absorption frequency is a function of the masses of the involved atoms and of the bond strength. This means, for example, that:

- two similar bonds involving the same atomic species but in different isotopes will have a different resonance frequency, due to the different masses involved;
- two similar atoms, bonded with a single, double or triple chemical bond, will have a different resonance frequency, due to the different strength of the bond;
- two similar atoms bonded with the same kind of bond but measured in a different environment can show a different resonance frequency, due to possible variations on the mobility of the atoms. A hydrogen bond on one of the two atoms involved in the resonant bond, for example, can result in a shift of the frequency.

Similar considerations, even if the model is slightly more complex, can be carried out for bending vibrations.

The strong dependence of the resonance wavelength from all the properties of the molecule and the environment allows revealing precise details about the fine structure of a substance through infrared absorption measurement. The infrared spectrum, therefore, act as a fingerprint of a particular system.

The idea behind infrared absorption spectroscopy is therefore simple and efficient: an infrared light beam is shot through a sample, and the transmitted intensity is measured as function of the wavelength. The frequencies at which the radiation is absorbed are indicative of the present chemical species. Unfortunately, the practical realization of the setup is slightly more difficult, due to the technological issues in the realization of the infrared-wavelength sensitive detectors.

Fourier transform infrared spectroscopy

Originally, infrared spectroscopy used to be performed via dispersive analysis: the frequencies emitted from the source are individually split, using a prism or a grating, and the diffraction figure is measured. Even if very powerful, this technique results to be either very rough or very slow: to obtain a good frequency resolution the diffraction cone must be enough wide, which means the detection system must move through a long path.

Fourier transform infrared spectroscopy results as a revolution in this field: it allows to provide a very precise measurement of the infrared absorption spectrum, which can be performed very fast and obtaining a large signal-to-noise ratio (SNR). The idea behind the FTIR apparatus is the use of a variable interferometer: the prism (or the grating) no longer needed, and therefore the detection part is fixed in place; the wavelength selection is made on the interferometer itself, upstream of the sample. Most of these apparatus are made by a beam splitter and two mirrors, in the Michelson-Morley layout: the first mirror is fixed in position while the second one can move, typically on a few millimeters rail. With this layout, the only moving part of the system is the second mirror, minimizing the possibilities of mechanical issues. When the beams recombine, according to the difference in the traveled paths, their different frequency components interfere in a constructive or destructive way [BH09; HG07].

The beam produced from the interferometer is then leaded through the sample and finally collected by the detector. The signal resulting from a detector placed after an interferometer is generally called *interferogram*: it represents the intensity of the recombined infrared beams as a function of the position of the moving mirror.

Let $f(k)$ be the amplitude of the waves reaching the interferometer as a function of the wave

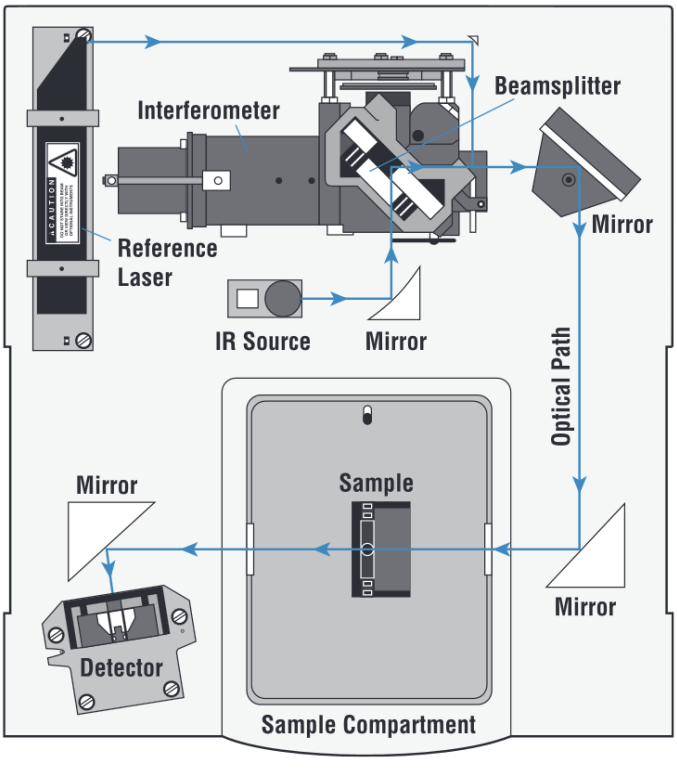

Figure 3.1: Scheme of a FTIR system. Figure from Thermo Scientific [The]

number; let for simplicity $f(k) = 0\,\forall k \leq 0$. Observe that the waves are supposed to be classically combined. The intensity of each wave is therefore:

$$I_0(k) = \big|A(k)\big|^2 = \big|f(k)\big|^2$$

which lead to a total intensity of:

$$I_0 \coloneqq \int_0^\infty \mathrm{d}k\, I_0(k) = \int_0^\infty \mathrm{d}k \big|f(k)\big|^2$$

Let's consider an ideal interferometer, with a 50/50 non-absorbing beam splitter and perfectly reflecting mirrors. Let x_1 be the total (go and back) length of the path through the fixed mirror, and x_2 be the total length of the path through the mobile one. Each couple of waves coming back from the paths can be written as*:

$$A_1(k; x_1) = f(k)e^{ikx_1} \qquad\qquad A_2(k; x_2) = f(k)e^{ikx_2}$$

and, after the recombination in the beamsplitter, they result in a wave with intensity:

$$A_{out}(k; x_1, x_2) = A_1(k) + A_2(k) = f(k)\left(e^{ikx_1} + e^{ikx_2}\right)$$
$$I_{out}(k; x_1, x_2) = \left|f(k)\left(e^{ikx_1} + e^{ikx_2}\right)\right|^2 = I_0(k)\left|1 + e^{ik(x_2 - x_1)}\right|^2$$

The total intensity measured by the detector is given by the sum of all waves:

$$I_{out}(x) = \int_0^\infty \mathrm{d}k\, I_0(k)\left|1 + e^{ikx}\right|^2$$

where, for clarity, has been defined $x \coloneqq x_2 - x_1$ (remember that x_1 is a constant).

To recall the intensity as a function of the wave number from the measured intensity, which is function of the mirror position, it is sufficient to carry out a Fourier transformation of $I_{out}(x)$. In fact, being $\kappa > 0$:

$$\begin{aligned}
\mathcal{F}\left[I_{out}(x)\right](\kappa) &= \int_{-\infty}^\infty \mathrm{d}x\, I_{out}(x)e^{-i\kappa x} \\
&= \int_{-\infty}^\infty \mathrm{d}x \int_0^\infty \mathrm{d}k\, I_0(k)\left|1 + e^{ikx}\right|^2 e^{-i\kappa x} \\
&= \int_{-\infty}^\infty \mathrm{d}x \int_0^\infty \mathrm{d}k\, I_0(k)\left(1 + e^{ikx}\right)\left(1 + e^{-ikx}\right)e^{-i\kappa x} \\
&= \int_{-\infty}^\infty \mathrm{d}x \int_0^\infty \mathrm{d}k\, I_0(k)\left(2e^{-i\kappa x} + e^{i(k-\kappa)x} + e^{-i(k+\kappa)x}\right)
\end{aligned}$$

Remembering that $\int_{-\infty}^\infty \mathrm{d}x\, e^{ikx} = \delta(k)$ and that $\kappa > 0$ it is straight forward to obtain:

$$\begin{aligned}
\mathcal{F}\left[I_{out}(x)\right](\kappa) &= \int_0^\infty \mathrm{d}k\, I_0(k)\left(2\delta(\kappa) + \delta(k - \kappa) + \delta(k + \kappa)\right) \\
&= I_0(\kappa) + I_0(-\kappa) = I_0(\kappa)
\end{aligned}$$

which confirms the hypothesis.

Therefore, it is sufficient to Fourier transform the signal obtained from the detector to find the frequencies spectrum, in which each frequency is associated with the intensity of the corresponding wave. Placing a sample between the interferometer and the detector, one can therefore easily detect which frequencies are absorbed, allowing to measure a full absorbance spectrum: the duration of the measurement is only determined by the time needed by the mirror to move. Typically, an acquisition can be made in less than a second. A full scheme of a FTIR system is reported in fig. 3.1.

*For symmetry, let's ignore the phase factors introduced by reflections

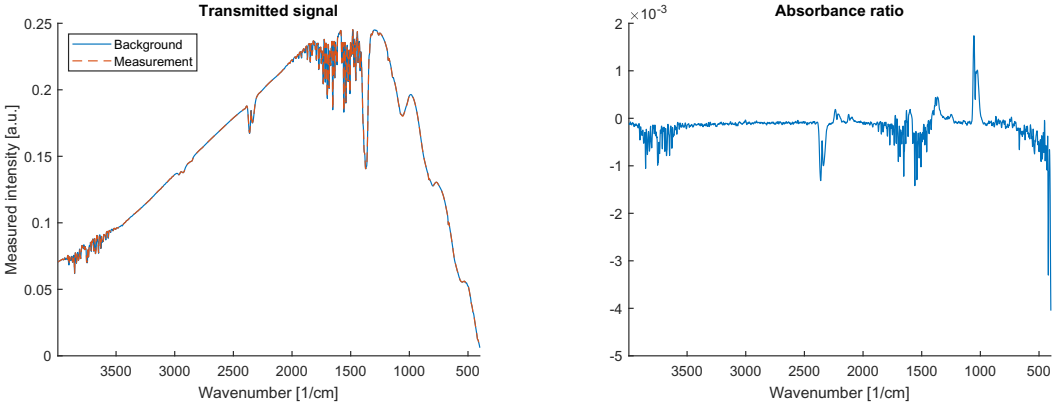

(a) Signal measured by the photodetector, after Fourier transorm

(b) Computed absorbance

Figure 3.2: The signal obtained from the FTIR. Note that in the right panel there seems not to be significant difference between the background and the measurements, but when the logarithm of the ratio is computed some clear peak appears.

Besides the gain in speed, other advantages make the FTIR system more powerful than the traditional infrared spectroscopy. Firstly, the instrument typically includes a laser as an internal wavelength reference: this means that it is self-calibrating, and never needs to be manually calibrated by the final user. Moreover, the absence of gratings and/or prisms allows to have a larger beam, and therefore a higher throughput of radiation: this results in an enhanced sensitivity.

Actually, FTIR systems are widely diffused and used in physics and chemistry laboratories all around the world.

Absorbance spectrum

The whole system, which includes also the windows and the surrounding air, is not totally transparent to the infrared beam and therefore a background signal must be considered. The procedure is pretty simple, remembering the shape of the Beer-Lambert law for light transmission: given a wave number k the intensity transmitted through a sample is

$$I(k) = I_0(k)e^{-\sigma(k)nd}$$

where $\sigma(k)$ is the absorption cross-section, n is the numeric density, d is the path length and $I_0(k)$ is the intensity entering the sample. If the density profile is not uniform along the line of sight (LOS), one should define an effective (nd) product, such that:

$$(nd)_{eff} \coloneqq \int_{LOS} n(x)\,\mathrm{d}x$$

When no sample is inserted in the system, the intensity transmitted depends only on the properties of the background:

$$I_b = I_0 e^{-\sigma_b n_b d_b}$$

where the subscript b characterizes quantities relative to the background and the explicit k dependence is hidden for clarity. Inserting the sample, and observing that cross-sections combine additively, one can write the intensity transmitted as:

$$I_s = I_0 e^{-\sigma_b n_b d_b - \sigma_s n_s d_s} = I_b e^{-\sigma_s n_s d_s}$$

where the subscript s quantities relative to the sample. All the information about the composition of the sample are therefore in the ratio between the intensity measured with the sample and the intensity measured in the background.

One can define the absorbance as:

$$A = -\log_{10} \frac{I_s}{I_b} = \kappa \sigma_s n_s d_s$$

where $\kappa = \log_{10} e \approx 0.434$ is a constant. Again, one can exploit the additivity of cross-sections to interpret the spectrum as the sum (weighted on the densities) of the cross-sections of the different chemical species present in the sample.

All this preliminary data processing, aimed to obtain the absorbance spectrum from the raw measurements, is carried out directly by the FTIR software. Summarizing, it:

- measures the intensity of the transmitted beam as a function of the mirror position, firstly in the background condition and then with the sample;
- Fourier transforms the spectra obtaining the intensity as a function of the wavelength (fig. 3.2(a));
- computes the absorbance, as minus the logarithm of the ratio between the intensities (fig. 3.2(b)).

The peaks in plot 3.2(b), therefore, correspond to peaks in the cross-sections functions, and can be related to a specific vibrational mode involving specific functional groups.

3.2 Experimental setup

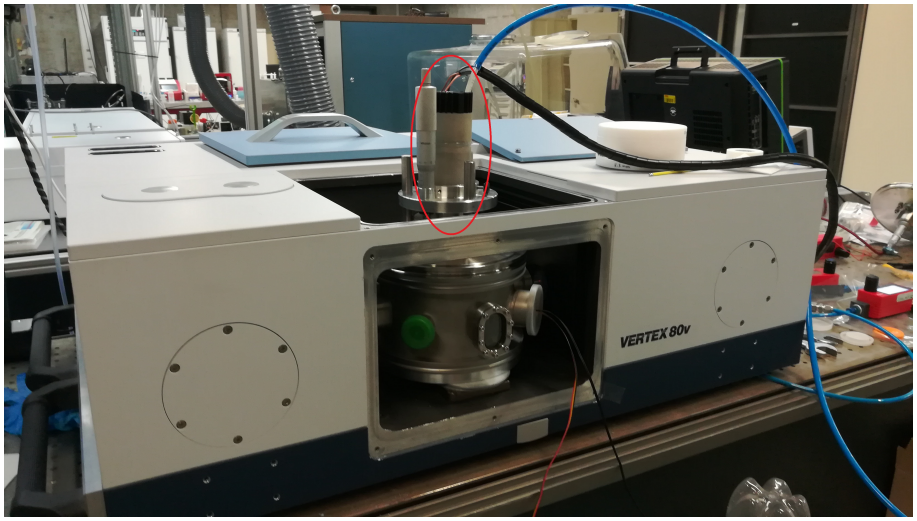

Figure 3.3: Experimental setup: the plasma source, highlighted, is contained inside a reactor, which is inside the FTIR sample compartment.

The spectrometer used for the measurements is a Vertex 80v, by Bruker. The instrumentation and the laboratories have been made available by the Basic Plasma Physics and Applications (BPPA) group in the Swiss Plasma Center (SPC) of the École polytechnique fédérale de Lausanne (EPFL). The system is designed to work in vacuum: the presence of air and atmospheric perturbations can damage the internal mechanical and optical components and introduce a strong noise on the signal. The PCC, instead, work in atmospheric air: a proper way to adapt the two systems must be studied.

The FTIR system is provided with a couple of flap windows, which split the whole system in two independent compartments: the apparatus compartment, which contain all the instrumentation, and the sample compartment, which can be easily accessed from outside. The windows are made in KBr, a material particularly transparent in the infrared spectrum, and can be opened when both the sample compartment and the apparatus one are in vacuum. With the flaps closed, one can keep the fragile components in vacuum and prevent damaging or dirtying them, while maintaining the

sample compartment free in atmosphere. The KBr windows are however fragile and are damaged by RONS: when they're left in contact with plasma, they can oxidize resulting in an opaque deposit on the surface and losing their transparency. The source, therefore, cannot be activated directly in front of them.

To isolate the PCC from the windows, a special reactor is designed. The cylindrical reactor, as can be seen in fig. 3.3, has been designed to be placed inside the sample compartment and it is provided with 8 different accesses. Two of them are closed with glass windows, to let the operator observe what is happening inside; four of them are technical accesses, typically closed with appropriate tip; the last two of them are provided with KBr windows, similar to the flap ones but way smaller. The reactor is aligned, using the reference laser available, such that the optical beam pass through the centers of the two KBr windows; even if these windows are subject to deposit and damaging as the flap one, being smaller they are cheaper and easily replaceable. Therefore, they can be used in contact with plasma, providing to replace them frequently.

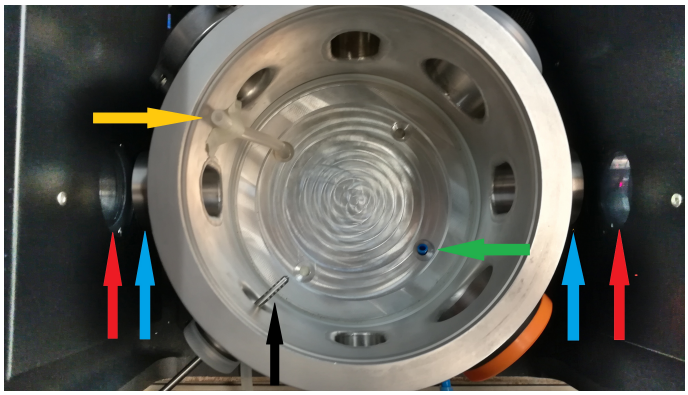

Figure 3.4: Internal of the reactor, top view. One can easily spot the spectrometer flap windows (red), the reactor windows (cyan), the gas inlet (yellow), the gas outlet (green) and the humidity meter probe (black).

The bioreactor itself is provided with a bottom plate which has four useful holes (fig. 3.4). One of them hosts the gas inflow pipe, used to provide the reactor with air from outside; this pipe, entering from the bottom plate, continues its path inside the reactor almost reaching its top. In this way, the air is injected in the reactor from above, allowing to properly mix with the helium coming out from the source and preventing gas stratification. On another hole of the bottom plate an outflow pipe is placed, whose other end is under extractor hood to capture all the residual chemicals inside the chamber. From one of the lateral accesses the probe of a temperature-humidity meter is inserted, in order to have a real-time measurement of these quantities inside the chamber. The holes and the windows not used are closed.

On the top of the bioreactor a custom lid is placed. The lid is designed to host the PCC source, and it is provided with a sliding seal and a micrometric screw which allows the source to be moved along the vertical axis. The source is inserted in the lid such that when the screw is in its lower position the nozzle tip is 4mm above the windows axis: this due to the fact that the light beam in the center of the bioreactor is estimated to have a diameter of 8mm. The shape of the lid, together with the positioning of the bioreactor, guarantees that the beam and the plume always meet perpendicularly and axially aligned (fig. 3.5).

The source is supplied with a pure helium flow, controlled using a *red-y* mass flow controlled by Vögtlin, specific for helium. A similar instrument, specific for air, is used to control the air flow inside the bioreactor, supplied with synthetic dry air ($80\%\,N_2$, $20\%\,O_2$). Finally, inside the reactor chamber the probe of a humidity sensor, Vaisala HUMICAP HM40, is placed: this allows to real-time measure the humidity and the temperature inside the chamber.

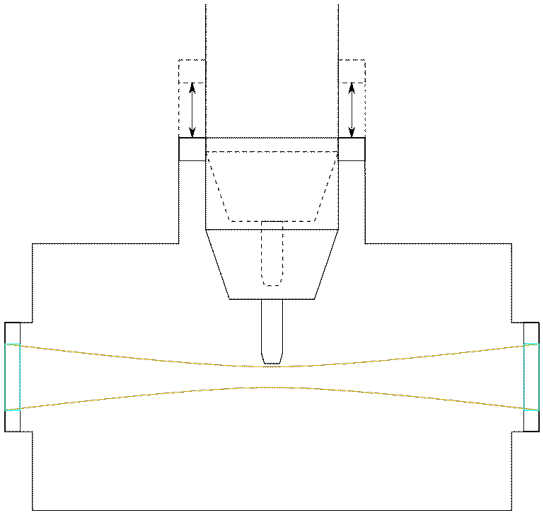

Figure 3.5: Scheme of the reactor and the position of the source; the beam path is also shown.

3.3 Control of the gases flows in the reactor

The PCC is meant to be used in open atmospheric air; it is of fundamental importance to properly tune the flows entering the reactor to simulate as good as possible the normal working conditions. In fact, if only the 2L/min he flow is injected, being it lighter than air and being the outflow in the bottom of the reactor the chamber will tend to saturate.

A study is conducted to observe the effects of the saturation on the plume: the source is placed inside the reactor with all the windows initially open and the helium flowing. As $t = 0$ is defined the moment when all the windows are closed, except for the bottom outflow, and pictures of the plume are taken every minute. The source is switched on only for a couple of seconds every minute, the time necessary to shoot the picture. All the pictures are acquired with a standard smartphone, with therefore no advanced regulations about focus and white balancing: the variations in color and intensity between different measurements sets cannot be considered significant, being strongly affected by camera automatic parameters adaption. The experiment is repeated for the three possible power regimes of the source.

The results of this first set of measurements are reported in figs. 3.6-3.8, and show interesting results: as the time passes and the reactor is saturated in helium, the plume disappears. It can be observed that, while in the first measures the plume is quite long, after some minutes it becomes more and more short until remaining trapped inside the nozzle. It can be therefore stated than the plume cannot properly develop in a saturated helium atmosphere, but needs air to manage to outflow the nozzle.

This is in total agreement with the theories about the development of the plume as a sequence of streamers. Inside the nozzle the helium plasma is always formed, where the effective dielectric barrier discharge happens. The streamers, instead, need the presence of an environment gas with higher breakdown voltage than helium, since they propagate in the mixing layer; if there is no air outside the nozzle, there is no mixing layer and the helium-air mixed streamer plasma cannot properly develop [BMR12].

The acquisition is then repeated injecting also an air flow. In addition to the 2L/min flow of helium from the source itself, a 1L/min flow of dry air is injected in the reactor, as previously described. The chosen value for the air flow is the maximum available from the production system. The results are reported in figs. 3.9-3.11. The protocol chosen is similar to the previous one: the first picture is taken with the reactor windows opened, while the second one after at least 10 minutes with all the windows closed and only the two inflows and the outflow. As can be observed, after 10 minutes of closed reactor there are no significant variations in the shape and the length of

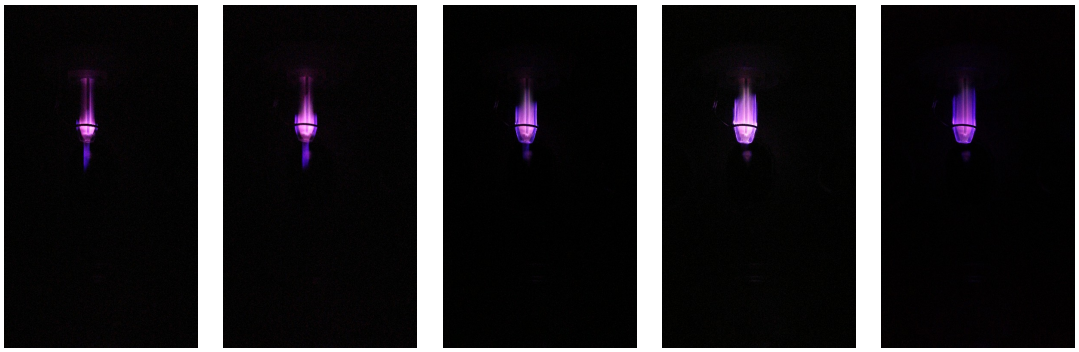

(a) 0 min (b) 1 min (c) 2 min (d) 3 min (e) 4 min

Figure 3.6: Only helium flow - Low power

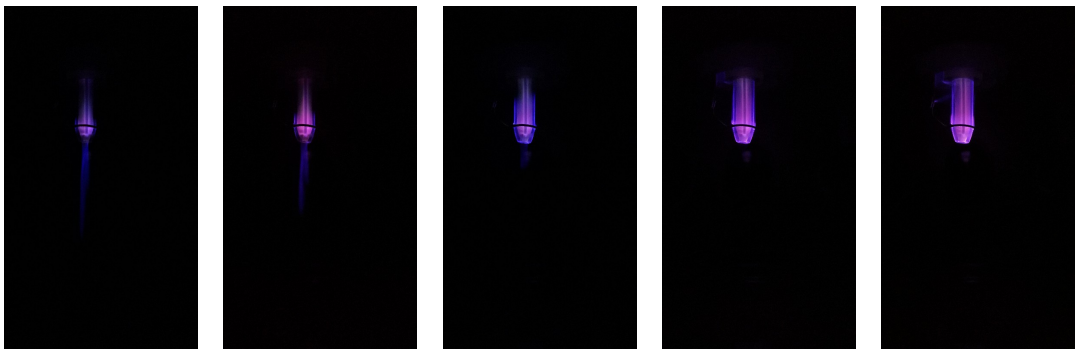

(a) 0 min (b) 1 min (c) 2 min (d) 3 min (e) 4 min

Figure 3.7: Only helium flow - Middle power

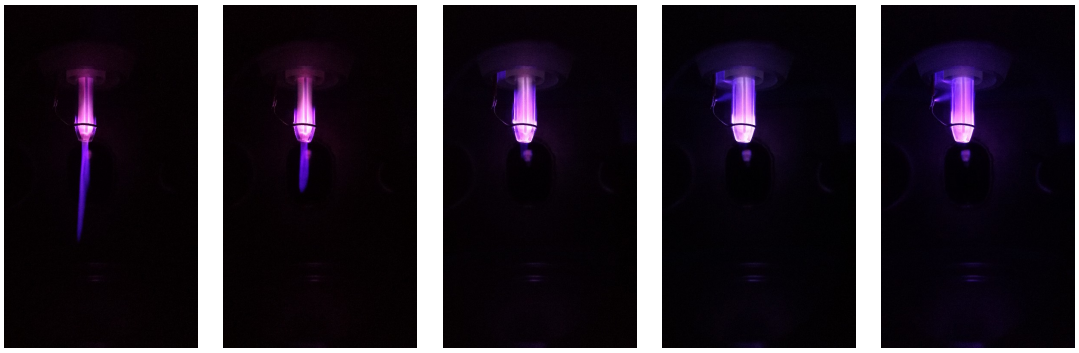

(a) 0 min (b) 1 min (c) 2 min (d) 3 min (e) 4 min

Figure 3.8: Only helium flow - High power. Note that the small triangle visible just below the nozzle is only the reflection on the window behind.

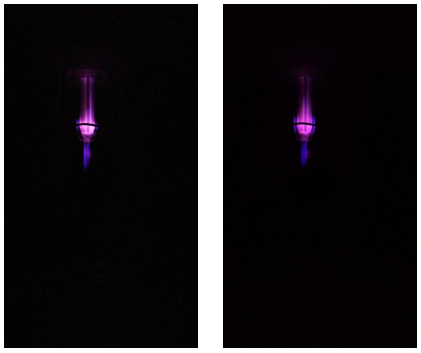

(a) 0 min (b) 10 min

Figure 3.9: Helium and air flows - Low power

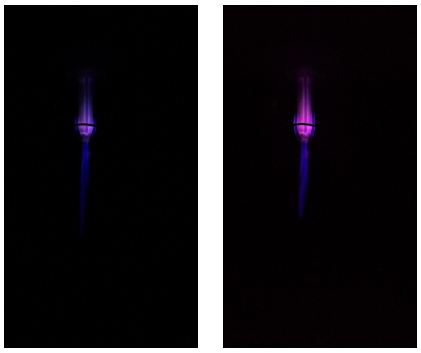

(a) 0 min (b) 10 min

Figure 3.10: Helium and air flows - Middle power

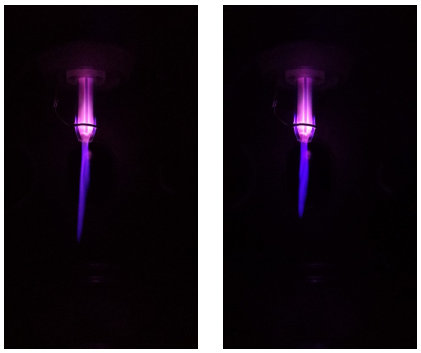

(a) 0 min (b) 10 min

Figure 3.11: Helium and air flows - High power

the plume. This result is particularly important, because it suggests that the chosen flow rate for air is sufficient to prevent the saturation of the chamber; moreover, it guarantees that the layout chosen for the air inflow is able to produce a proper mix of air and helium, preventing stratification effects.

During these studies about the flow, using the Vaisala probe, temperature and humidity have been tested in different points of the reactor and at different heights. No significant differences have been detected either in temperature or in humidity. Remembering that the latter is indicative of the local proportion between helium and air, this suggests that there are no significant inhomogeneities inside the reactor.

Combining the last results it can be stated that, thanks to the flows, air and helium properly mix inside the bioreactor: in the following, therefore, it has always been considered the reactor containing a homogeneous gases mixture.

3.4 Control of the temperature inside the reactor

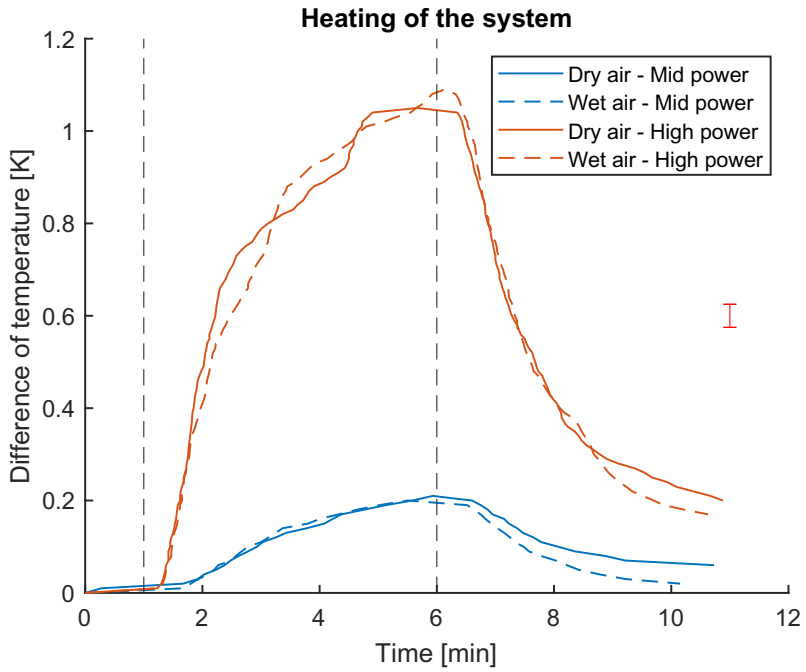

Figure 3.12: Heating of the air inside the reactor, for middle and high power and for dry and wet air. The source is active from $t = 1$min to $t = 6$min (dotted vertical lines). The instrument manufacturer does not provide an error for relative measurements; however, repeated measurements suggest that the random error component is in the order of the red marker represented in the side of the plot (not reported in each point for clarity).

The setup built since now allows verifying, at least roughly, the effective coldness of the plasma produced by the source, namely the total quantity of heat delivered by the source to the surrounding atmosphere, for example via body ohmic heating, via plasma collisional heating and via afterglow exothermic reactions. The reactor is closed, with the Vaisala temperature and humidity sensor inside, and the flows of air and helium are switched on. When equilibrium of measured humidity and temperature is reached, the source is switched on for 5min and the temperature in the chamber is monitored during and after the discharge. The results, in terms of difference of temperature with respect to the equilibrium one, are reported in fig. 3.12.

It must be pointed out that these measurements are purely indicative: the gas inside the chamber is continuously changing and the outflow results in a heat sink. In fact, the volume of the reactor can be estimated around 1.7L, and the total influx (of air and helium) is 3L/min.

However, as expected, the variation in temperature is quite small. The low power configuration measurements are not reported since its effects are below the system sensibility; for the mid power, the maximum temperature difference after 5 minutes of source operation is around 0.3K while for the high power is about 1.1K. These values are definitely low, considering also that in a typical biological study the PCC treatment time does not overcome 3min.

Measurements are repeated multiple times in the same conditions, verifying reproducibility; moreover, the tests are carried out both injecting dry or wet air (respectively, 0% and 75% of relative humidity). The results are totally comparable: no significant differences have been detected, at least with the sensitivity of the available instrumentation.

The FTIR system with the PCC is now available to acquire the first data. Before taking efficient measurements, however, an optimization process must be carried out.

Chapter 4

Diagnostic system optimization

The core of this thesis work is related to the optimization of the experimental setup. The smallness of the source and the low quantity of produced RONS, as well as the necessity of working in atmosphere, result in a set of issues and noise sources that must be reduced to obtain a clean acquisition.

In the following, the first spectra are shown, pointing out the main issues; the actions undertaken to optimize the system are then explained in details; finally, the results reached in terms of noise reduction are exposed.

4.1 First acquisition and setup issues

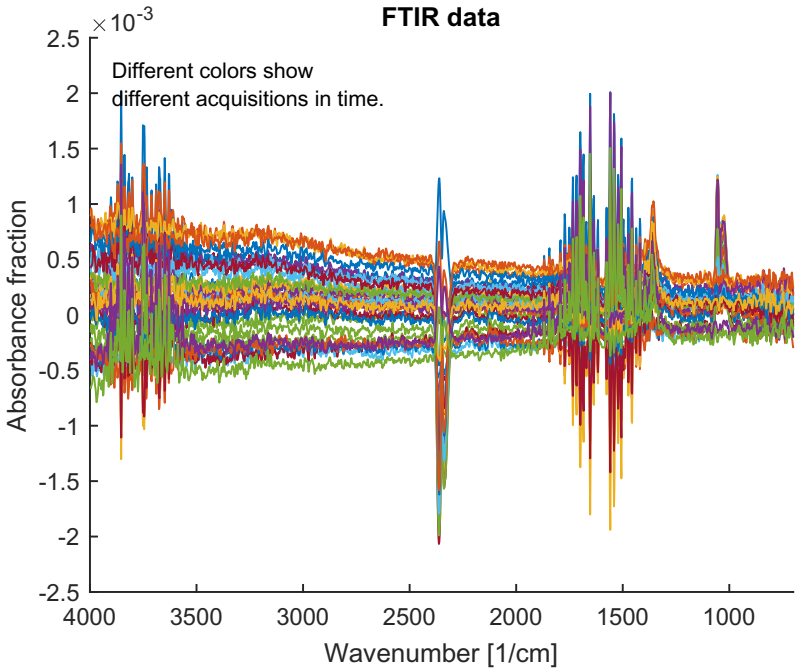

Figure 4.1: One of the first set of spectra acquired. Different colors label different acquisitions in time.

The FTIR system is, in principle, pretty flexible. The available instrument nominally has a spectral range from 5cm^{-1} to 50000cm^{-1} and a resolution that can reach 0.2cm^{-1} [Bru]. The time needed to acquire a spectrum is proportional to the wideness and the resolution required: a set of parameters that meet the quality requirements and the fastness ones must be chosen. To

include all the interesting peaks plus a reference region, spectra have been acquired in the range $700 - 4000\text{cm}^{-1}$, which also corresponds to the optimal transparency band of the KBr windows. Also, considered the width of the interesting peaks, it has been chosen to use a resolution of 4cm^{-1}. To prevent noise fluctuations and reduce the random error, moreover, each spectrum is the result of an average over 16 scans: this means that for each measurement the mobile mirror of the interferometer travels across its path 16 times. With this set of parameters each measurement lasts about 17s: more or less a second for each mirror scan. It has also been observed that the FTIR apparatus is subject to stress: if a set of acquisition is carried out in rapid sequence the noise slightly rises. To prevent this effect, it has been chosen to wait at least 10s between two subsequent acquisitions.

In fig. 4.1 is reported one of the first set of spectra acquired. The whole system is set up, the fluxes are opened, the PCC is switched on and a set of spectra is measured, starting an acquisition every about 30s. This first result is very noisy and does not allow making considerations about the produced RONS. The main issues that can be recognized are:

- the baseline. Expected to be constant, it is continuously and randomly shifting and tilting, introducing a very high noise on the measurements. Without a proper defined baseline, peaks cannot be recognized and measured;
- the water peaks. The two broad peaks around 4000 and 1500cm^{-1} are very strong, and prevent from correctly observing other peaks in that area;
- the low signal. An absorbance fraction of 10^{-3} is near to the detection limit of the instrument.

To correct these issues, both hardware and software improvements have been studies, tested and applied.

4.2 Windows effects on the baseline and on the signal noise

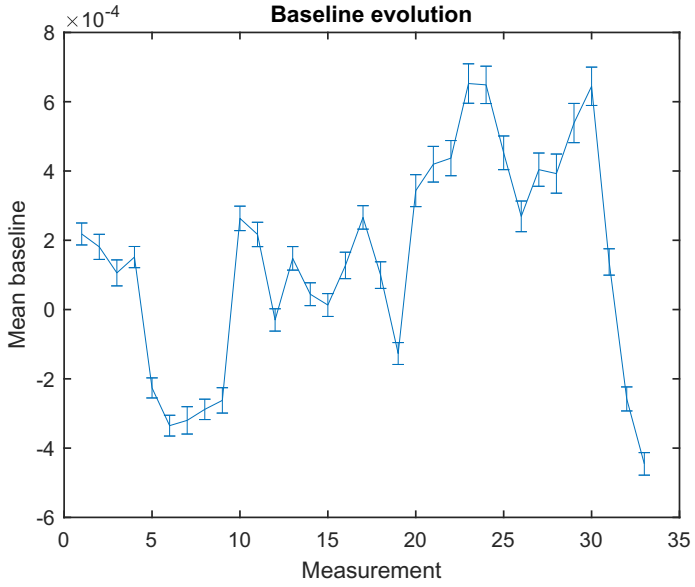

Figure 4.2: Mean value of the acquired spectra in the interval $2800 - 3200\text{cm}^{-1}$, in a sequence of measurements (one every about 30s). There is not an evident evolution trend.

As a first issue, the shifting of the baseline has been studied. Let's focus on the interval between 2800 and 3200cm^{-1}: in that area no peaks are expected to be present, and therefore a flat negligible baseline is predicted. Computing an average height of the baseline for different subsequential measurements performed at intervals of about 30s, the plot in fig. 4.2 is built.

From this first plot, and from similar plots realized for different datasets, there is not a defined trend for the evolution of the baseline in time. One can therefore state, at least for the time

resolution available, that the baseline evolves stochastically without a preferred trend. This can suggest, from a physical point of view, that the shift and the tilt are simply due to random noise introduced by the components and cannot be ascribed to a drift phenomenon.

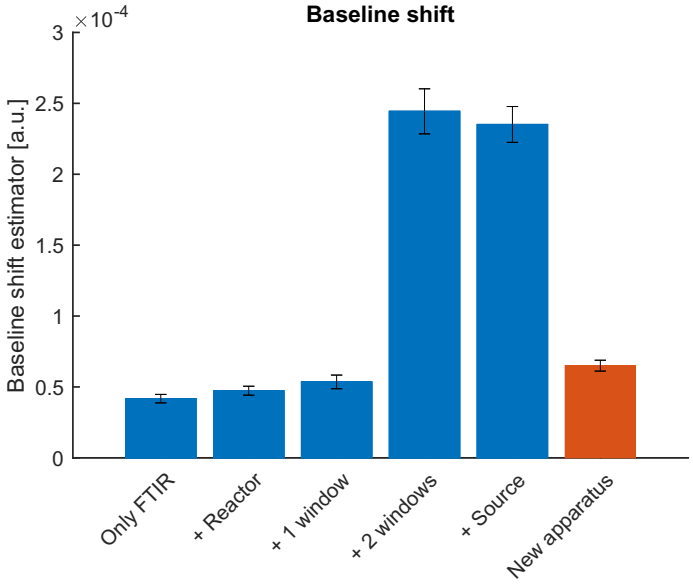

Figure 4.3: Evolution of the baseline noise when each component is added, and value obtained after windows replacement.

To find the origin of the noise, the setup components are mounted one by one and a set of spectra is acquired after each module is added. The baseline shift is then quantified using the standard deviation over 10 subsequent spectra of the mean absorbance measured in the cited wavenumbers interval. The results are reported in fig. 4.3. As can be seen, the main aggravation of the noise can be ascribed to the insertion of the second window in the reactor: the KBr small windows, therefore, can be recognized as the main sources of the baseline shift.

It is interesting to observe also the intensity of the signal detected by the system. Passing through the small windows of the reactor, the more external annulus of the beam is totally cut out and part of the intensity of the transmitted light is absorbed by the windows themselves. While the first effect is structural, depends on the shape of the windows and of their supports and cannot be easily corrected, the second one can be reduced frequently replacing the windows with new and polished ones. Let's consider the raw value of intensity measured, before normalizing it to the background: in fig. 4.4 this value is reported, averaged over about 10 acquisitions and normalized to the *Only FTIR* case. As can be seen, the bioreactor does not reduce significantly the signal; instead, the two windows strongly reduce (about 30% each one) the intensity of the transmitted beam, and also the presence of the lid with the source is visible. In the end, the intensity of the beam detected is reduced by the whole setup to less than 40% of the initially available one. Given the very low signal available, it is of interest to minimize the intensity losses, to fully exploit the sensitivity of the detector.

The results obtained from the last two plots strongly highlight the importance of clean and polished windows for the bioreactor. Old or opaque windows can strongly reduce the signal and introduce an important noise. The first significant improvement on the setup, therefore, has been obtained replacing the bioreactor windows with new ones. During the operations, moreover, a small crap has been detected on one of the FTIR flap windows, which separates the vacuum section from the atmosphere: it was probably due to the difference in pressure and therefore to the mechanical stress of the window itself. However, a new window has been purchased from the FTIR company and the broken one has been replaced.

In the previous plots (figs. 4.3 and 4.4) also the data relative to the setup with the new windows are reported, labelled as *New apparatus*. It can be observed that, with the new windows, the baseline shift is comparable to the one obtained with only the FTIR. Moreover, regarding the

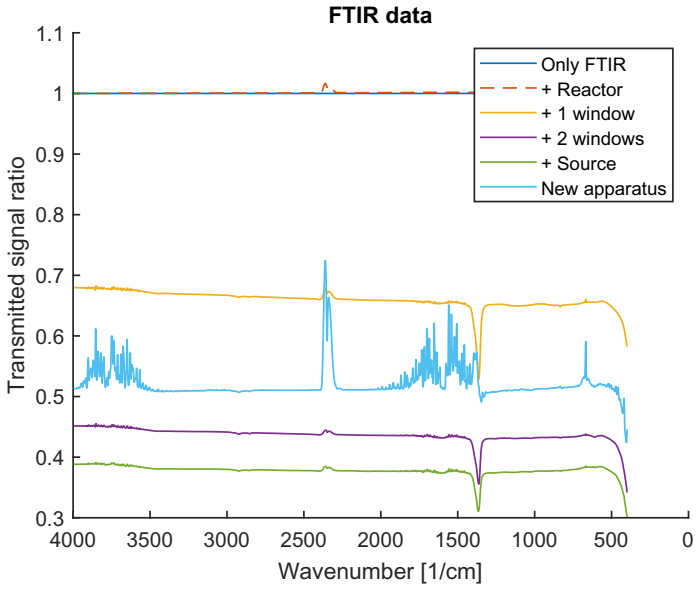

Figure 4.4: Intensity measured by the FTIR detector, as function of the wavelength, when each component is added, and after windows replacement. The curves are normalized to the *Only FTIR* one.

transmitted power, with the final setup it can be observed to be more than 50% of the initially available one. It is clear, therefore, that the hardware replacement come out in a significant improving of the obtained signal: windows must therefore be continuously checked and replaced (or re-polished) regularly after usage.

4.3 Control and injection of humid air

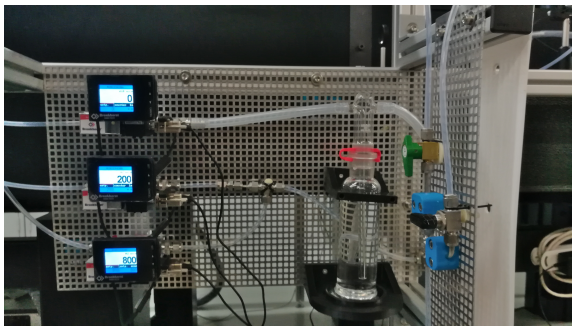

Figure 4.5: The humid air production system: from top to bottom, the flow meters for air (which goes through the bubbler), oxygen and nitrogen.

The injection of humid air in the bioreactor is guaranteed by a specific humid air production system (fig. 4.5). The system is fed with three different gases: nitrogen, oxygen and dry synthetic air, each one provided with a flow meter. The dry air is flown through a bubbler that humidify it, and mixed with the other gases: the result is a flow of maximum 1L/min of air whose humidity can be easily regulated. All the mixing between gases are made using *mixing chambers*, which guarantee a correct merging of the fluxes even if their magnitude is different. The system is build such that also the ratio between oxygen and nitrogen in the dry component can be changed; however, for the purpose of this work, the standard proportion $(1:4)$ has always been considered.

The humidity is always measured in terms of *relative humidity (RH)*, defined as the ratio of the partial pressure of water vapor over the vapor pressure of water in air; an ideal bubbler is able

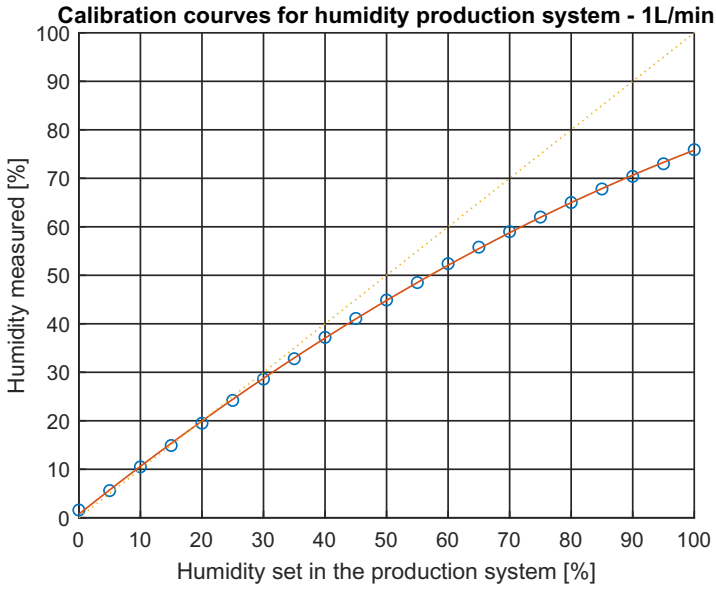

Figure 4.6: Calibration curve. Dots mark datapoints, while the red line shows the best fit.

to produce vapor-saturated air, which means with relative humidity 100%. Being RH the desired relative humidity, the fluxes for each gas are then set as:

$$Q_{O_2} = 0.2 \cdot (1 - RH) \cdot 1\text{L/min}$$
$$Q_{N_2} = 0.8 \cdot (1 - RH) \cdot 1\text{L/min}$$
$$Q_{\text{Bubbler}} = RH \cdot 1\text{L/min}$$

The efficiency of the real bubbler, however, is not perfect: therefore, the apparatus needs to be calibrated before use. A small chamber is connected to the outflow of the mixing system and, using the Vaisala HUMICAP HM40 humidity meter, the asymptotic humidity value inside the chamber has been measured as function of the RH set in the production system. The results, reported in fig. 4.6, allow to compute the real humidity of the air obtained as function of the RH set in the flow meters. The plot, as expected, shows that for low humidity the measured value coincide with the expected one; as the humidity rises, however, there is a loss of efficiency of the bubbler due to the high flux inside, which results in a real humidity slightly lower than the expected one. The reproducibility of these calibration data has been successfully verified with different scans in different days.

Observe that similar measurements cannot be performed live during the FTIR scans, since in the bioreactor there is also the flux of helium which false humidity values. Roughly, the humidity measured during the acquisitions is observed to be around a third of the expected one: this is totally meaningful, fluxing in the chamber 1L/min of air and 2L/min of helium, and therefore being the air around a third of the final mixture composition.

4.4 Digital data processing after acquisition

Even if the upgrades in the hardware give a strong improvement on the signal, some issues still remain affecting the measurements. To clean the remaining noise, a post-processing MATLAB routine has been set up. The script can be divided in two steps:

Baseline alignment The baseline of the signal still suffers from a small shifting and tilting. To properly detect and align the baseline, a second degree polynomial is used. As references, it has been chosen to use the peaks of ozone and carbon dioxide, together with the already

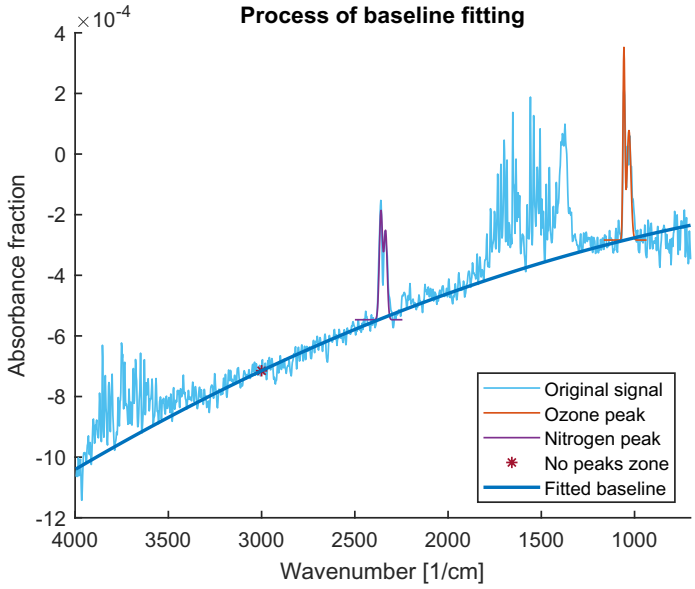

Figure 4.7: Process for the fit of the baseline: one can see the raw data, the two peaks and the point used for the baseline detection, and the fit baseline.

recognized no-peaks zone. Both the peaks have a double tip, and therefore they're fit using a couple of Gaussians over a constant shift:

$$f(x) = c + a_1 \cdot \exp\left\{-\frac{(x-x_1)^2}{s_1}\right\} + a_2 \cdot \exp\left\{-\frac{(x-x_2)^2}{s_2}\right\}$$

where x_1 and x_2 are fixed to the known positions of the peaks while c, a_1, a_2, s_1 and s_2 are the fit parameters. From the fits, the heights of the peak basis are achieved (c) and combined with the absorbance measured around 3000cm^{-1}, where no peaks are expected to be present. With these three points a parabola is computed, representing the baseline of the signal (see fig. 4.7). Subtracting the obtained polynomial from the signal, an aligned spectrum is obtained. One must highlight that this process is not safe from errors: the three points used to estimate the parabola have themselves an error, which is propagated during the baseline subtraction and tracked for the final estimation of the errors on the peaks heights.

Water cleaning Even waiting for system stabilization and avoiding all movements in the laboratory, some small perturbations in the atmosphere in the gap between the bioreactor windows and the FTIR ones are still present, resulting in small changes of water and carbon dioxide concentrations. Since for both compounds molar absorbance is quite high, even a small inhomogeneity can result in a large noise in spectra. The CO_2 peak is very sharp and localized and does not interfere with other peaks; H_2O, instead, have wide peaks bands which overlap with other peaks hiding them. The second section of the script is therefore devoted to removing water noise from spectra. Some acquisitions with only humidity variations have been performed in advance and a reference spectrum for water is built. Comparing it with each acquired spectrum, and in particular averaging the ratio between the height of the peaks in the reference spectrum and in the acquired ones, a magnitude for the presence of water is computed. The reference spectrum, properly rescaled with the obtained factor, is then subtracted to the acquired one. In this way the noise due to presence of water is almost totally removed, allowing to see peaks from other gases in the same wavelength region.

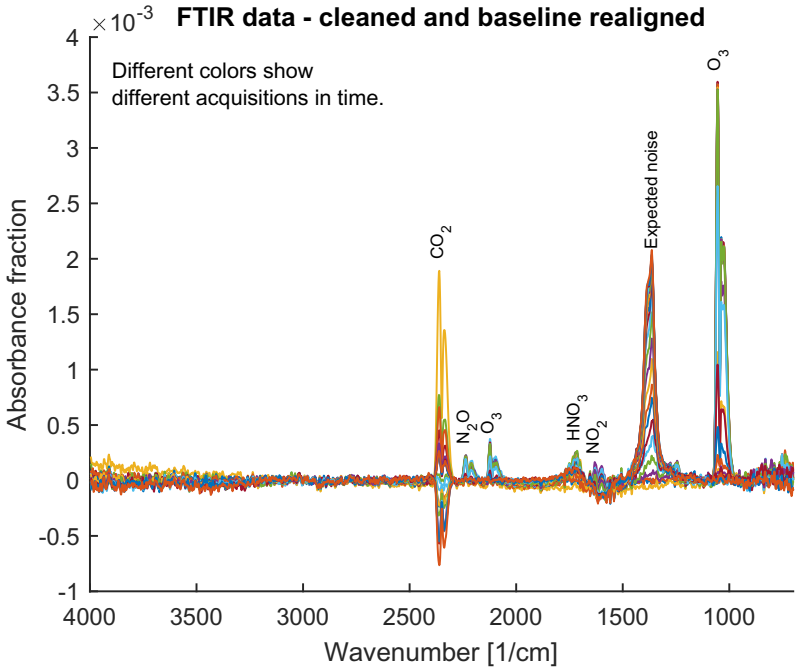

Figure 4.8: Spectra acquired with PCC in high power configuration and dry air, after all the optimization process. Various peaks from different gases are clearly visible.

4.5 Detected gases

The combination of both physical and post-processing modifications of the setup leads to a strong improvement of the acquired signal. In fig. 4.8 a set of spectra acquired with the PCC in its high power configuration and using a 2L/min helium flow and 1L/min dry air flow can be seen. The results of the hardware and the post-processing improvements are evident: the spectra are definitely more clean and clear with respect to the ones shown at the beginning of the chapter.

In fig. 4.8 the first important result of this thesis work can be recognized. The emergence of various peaks as a consequence of the PCC activity is a strong evidence that there is a triggering of chemical reactions and a real production of active species, interacting both with oxygen and nitrogen in the air. The main gases that can be recognized are:

O_3 The ozone peak is no doubt the most significant: it is clearly visible and high, and also its first overtone can be clearly seen.

N_2O AND HNO_3 Both nitrous oxide and nitric acid peaks can be identified, but their magnitude are an order of magnitude smaller with respect to the ozone one.

NO_2 A small peak that can be recognized in nitrogen dioxide seems to be present; however, the peak is very small and it is in the middle of the broad water mark.

In the spectra two other peaks appear. The first one can be identified in the resonance of the CO_2: as for water, carbon dioxide is normally present in ambient air and small variations of its concentration due to respiration or movements are unpredictable. Secondly, another big peak (labelled *Expected noise* in the plot) is visible and growing in time. This peak has been recognized in the reactions of RONS and the interactions of plasma with the KBr of the windows: potassium and bromine can form oxides and other compounds that deposit on the windows themselves creating the visible absorption peak.

The detected peaks can be related to the biological effects of the source. Ozone is well known as a disinfecting agent: it has been observed to be particularly effective in purification and contaminants removing. Being a reactive oxidizing species, its effectiveness as a bactericide is commonly ascribed to its interference with cellular redox equilibrium; the presence of ozone can lead to oxidative

stress, and therefore to apoptosis. Wound healing, instead, is typically connected to the presence of NO, and in general of nitrogen and oxygen compounds, in the environment. As previously explained, the presence of RONS can trigger both the formation of fibrinogen clusters and the stimulation of albumin or immunoglobulin G aggregation. The presence of N_2O and HNO_3 in the source, therefore, can be related to the wound healing and the blood coagulation effects. A special consideration must be done regarding nitrogen dioxide NO_2: it is an irritating and potentially fatal compound, so its production must be kept under control.

4.6 Fitting of the peaks and gases quantities estimation

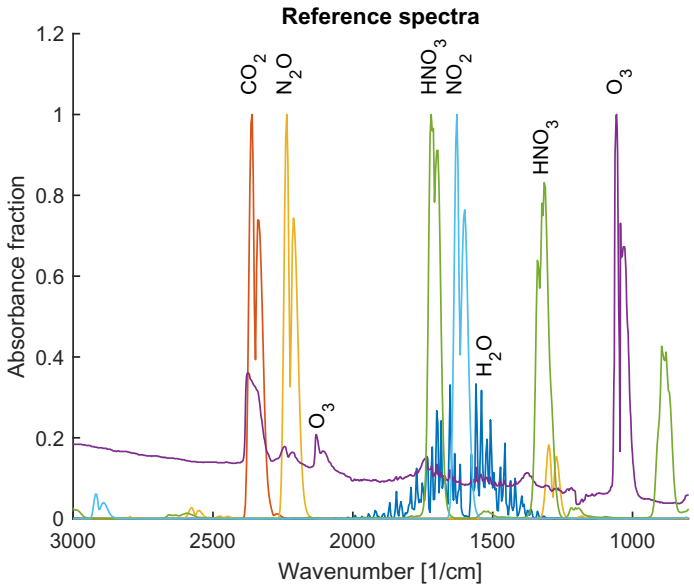

Figure 4.9: Reference spectra for various gases. For the ozone, the only meaningful peaks are the labelled ones; the broad shoulder and the other peaks are due to the method used to acquire the spectrum, and they're not related to the ozone itself.

To properly detect the peaks a set of reference spectra has been collected, provided partially by the FTIR company, Bruker, and partially from the Chemistry WebBook by the National Institute of Standards and Technology (NIST) [Nat]. The reference spectra are only qualitative, showing the position and the shape of the peaks, but they do not allow to compute a quantitative estimation of the densities inside the chamber. The measured height of each peak is related to the density integrated over the line of sight, and therefore depends both on the geometry of the reactor and the density profile inside the chamber. Moreover, especially for ozone, it is particularly difficult to associate the peak area with the real ozone concentration, and calibrated reference spectra seems not to be available in public literature.

The usage of the FTIR system to make quantitative analysis would require a proper calibration with instruments that were not available in the laboratory; however with the available setup relative quantities can be measured and variations can be efficiently detected.

It is worth observing that this means also that, even if in fig. 4.8 the ozone peak is way larger than the other ones, it is not guaranteed that the density of ozone is higher than the density of nitrous oxide and/or nitric acid. Comparisons can be correctly made between peaks of the same gas in different conditions (without changing the system geometry), but not between different gases.

From fig. 4.9 one can immediately observe that peaks are essentially not overlapping: the main gases expected to be present in the chamber, except for the wide peak of the water, have their peaks well separated. This allows to use an integral to quantify the size of the peaks: the presence of each gas, here and in the following, is defined as *the integral of the acquired spectra over the domain in which the reference spectra overcome half of its maximum value*. A small exception is

made for HNO_3: its spectrum shows two main peaks, but the smallest one is totally inside the huge peak from the windows oxidation. To avoid confusing the two signals, for HNO_3 quantification the integrals have been performed only on the higher peak.

Having the system optimized and a protocol for the measurement of spectra defined, comparison between different acquisition can be now carried out varying the system conditions.

Chapter 5

Scans in parameters space

The flexibility of the setup allows to easily change two parameters of the system: the vertical position of the source, which can be lifted or dropped, and the humidity of the air injected in the reactor. From a biomedical point of view, to understand the possible variability of RONS production is of fundamental interest: on one side, it is important to define the optimal distance between nozzle and substrate for different kind of treatments; on the other side, one should remember that the air humidity is typically not a tunable parameter in a medical application and if significant differences are detected in the plume behavior one should define different application protocols as function of the environmental humidity.

With the available setup, even if absolute densities cannot be computed, one can observe variations in the integrated concentration of various gases. Particularly for ozone, whose peak is high and clean, variations can be observed as function of the system parameters.

5.1 Data acquisition protocol

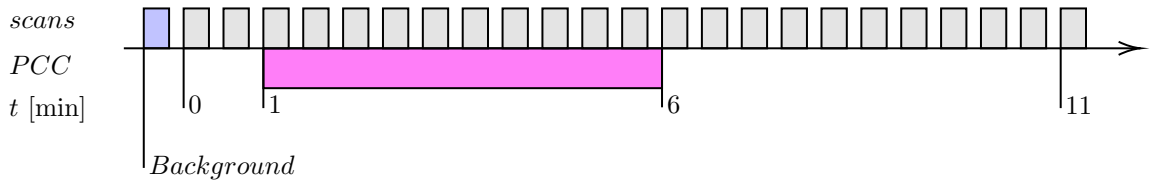

Figure 5.1: Data acquisition protocol.

To acquire uniform datasets and avoid effects from uncontrolled parameters, a strict data acquisition protocol has been defined.

Given the fact that each acquisition lasts about 17s, it has been chosen to acquire spectra at regular intervals of 30s using the automatic *repeated measurement* program of the FTIR system. In this way, on one hand overlapping between acquisitions and stressing of the system are avoided, but at the same time a good temporal resolution is obtained.

Before starting each acquisition, air and helium fluxes are switched on and the system is left to stabilize. Thanks to the presence of the humidity and temperature sensor inside the reactor, a useful indication of the stability of the system is available. The system is considered stable when the sensor does not register a variation of temperature and humidity (sensibility ± 0.01°C, ± 0.01%RH) for at least two minutes.

The spectra acquisition then proceeds as following:

- first, acquire the background;
- after 30s, start the FTIR measurements ($t = 0$): use the automatic repeated measurement, 23 measurement with a 30s cadence;
- at $t = 1$min switch on the PCC, with a timer of 300s;

- at $t = 6$min, therefore, the PCC goes off;
- at $t = 11$min the last spectra acquisition start.

In the following the results of each acquisition is associated to the starting time of the acquisition itself. One must remember, however, that the results are averaged over the following 17s. This means that, for example, in the acquisition at $t = 1$min the RONS rising is expected to be already clearly visible as well as their decay in the $t = 6$min one.

Defined the protocol, some scans are performed, varying the position of the source and the humidity of the injected air. Particular attention has been paid to the reproducibility of the results: all the reported data have been verified repeating the scans in different days and following different orders in parameters space exploration.

This means that, for example, if the first day the spectra are acquired following the order *low power - middle power - high power*, the next day they're re-acquired in the reverse order; same for rising and lowering humidity and for lifting or dropping the source. For most time-consuming scans, check scans are performed with less resolution or acquiring less datapoints, but always enough to allow a compatibility checks. This guarantees that the measured variations in RONS production are really related to the chosen parameter, and not to other effects due to measurement method.

Observe that, when compatibility checks are performed, one must focus on the ratios between the different measured values and not on the absolute values of peaks integrals: the heights of the peaks, as previously reported, are strongly related to the geometry of the system. Since the setup is disassembled every evening and reassembled every morning, so that when not used the FTIR can be sealed and left under vacuum to minimize the effects of atmosphere on the delicate internal mechanics, the positioning of the reactor can slightly change and therefore the heights of the peaks can marginally vary.

In all the scans performed, the repeated measurements confirm the first results, and no issue on reproducibility has been found. For clarity, in the following data from only the most resolved scan of each type are shown.

5.2 Scans along the height of the plume

The first scans performed are along the plume, at different source powers. Remembering that the diameter of the beam in the center of the reactor can be estimated around 8mm, the distance of the nozzle from the beam axis has been varied from 4mm to 34mm with a step of 10mm; in all the positions, the production of RONS has been measured in low, middle and high power configuration. As previously described, the magnitude of each peak is estimated via the integral, and the results for ozone are reported in fig. 5.2: the trend of the data is clear. One can easily observe that, as the PCC is switched on ($t = 1$min), the peak magnitude starts to rise and reaches a stable value in about 2 minutes. Then, when the PCC is switched off, an exponential decay of the concentration is visible, and the integrated absorption returns to negligible value.

To estimate an asymptotic value for the absorption itself a *stability interval* has been individuated (highlighted by dashed lines) in which the measured values are averaged. The results are reported in fig. 5.3, as functions of power and height.

Regarding the errors, two main sources affect the estimated asymptotic value, whose contribute are quadratically summed to obtain the error on each data point. The first one is connected to the time average, and it is simply computed as the standard deviation of the integrated absorbance in the stability interval. The second one, instead, is ascribed to the noise of the acquired spectra. In particular, this contributes combine the intrinsic noise of the FTIR signal and the uncertainty on the baseline used for the correction of the spectra. To properly recognize the source of the errors, in fig. 5.3 and in the similar following ones, above the total error a second (smaller) error bar is reported in red: this marker represents the contribution to the total error given by the second source just described.

As can be seen, in the height-power scan the error is almost totally due to the spectra noise, suggesting that the ozone concentration reaches a very stable value in the averaged interval.

The immediate result from the high-power scan regards the importance of the power configuration of the PCC. As shown by the plot, the production of ozone is significantly different at low, mid and high power. In particular, between the low and the high power there is a factor of more

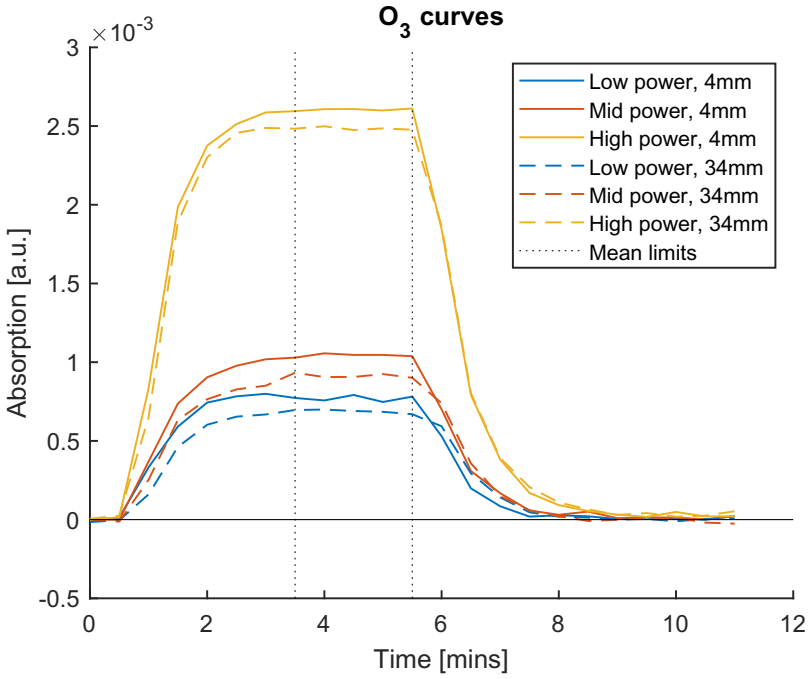

Figure 5.2: Integrated absorption of the ozone at different powers and moving along the plume. The dashed vertical lines highlight the interval averaged for computing the estimated asymptotic value. Different colors show different power regime and different heights; error bars are not shown for clarity, refer to fig. 5.3.

than three, which means that (being the reactor geometry constant and supposing that the density profile inside the reactor maintains its distribution) for high power the ozone production is almost tripled with respect to low power.

The second result is that the measured quantity is almost uniform along the plume. Except for the first point, just below the nozzle, in which the ozone concentration is slightly higher, it remains constant (inside the experimental error) along the plume height. Unfortunately, the variables affecting this measure are a lot and different (from the geometry of the reactor, to the motion of the ozone inside the reactor itself), so no strong claims can be done on the ozone production along the plume.

Regarding other gases, their peaks are too small to observe a significant trend. In fig. 5.4 the equivalent plot for nitrous oxide is reported: similarly to the ozone plot, a different level of production for the different powers can be intuited, but the differences are below experimental error and cannot therefore be considered significant.

5.3 Scans over the environmental humidity

The second large set of scans have been performed varying the humidity of the air injected in the chamber. The whole spectra of available humidities has been explored, with a resolution of about 10%, and with the three available power configurations. The results are reported in figs. 5.5 and 5.6, where the humidity on the horizontal scale is the real value for the injected air obtained thanks to the calibration done in the previous chapter.

Again, it is clear that the three power configurations result in three different levels of ozone production: the found values with dry air are proportional to the one previously measured.

The variation of the ozone concentration as function of the humidity shows a clear trend. As the quantity of water vapor in the air rises, in fact, the resulting concentration of ozone falls down. When the humidity shifts from 0% to 75%, in the high power configuration the ozone concentration becomes less than half. The effect, moreover, is different for the different power configuration: in table 5.1 are reported the ratios between the measured integrated absorptions

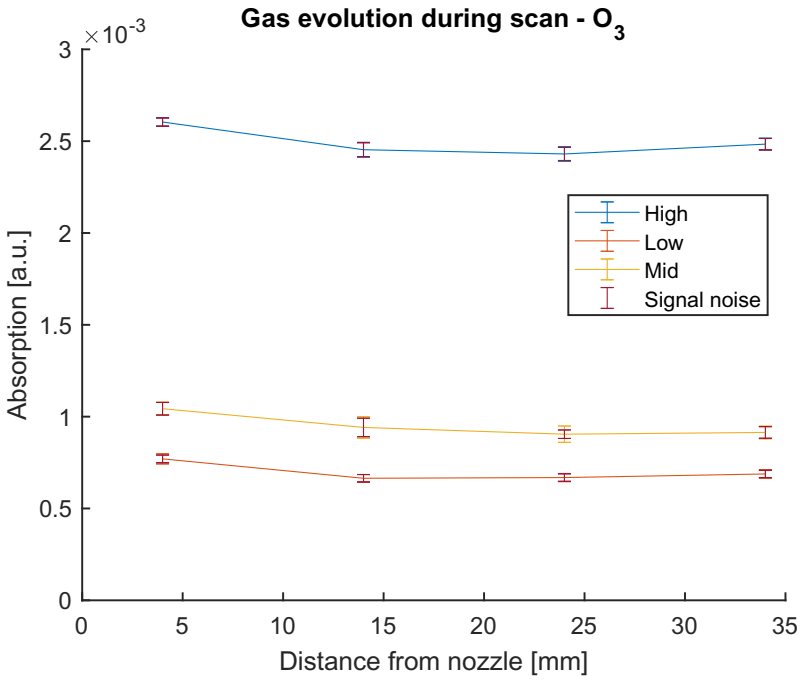

Figure 5.3: Estimated asymptotic value of the ozone concentration, in terms of integrated absorption, at different power configurations and as function of the distance from nozzle. See the text for the meaning of the red bars.

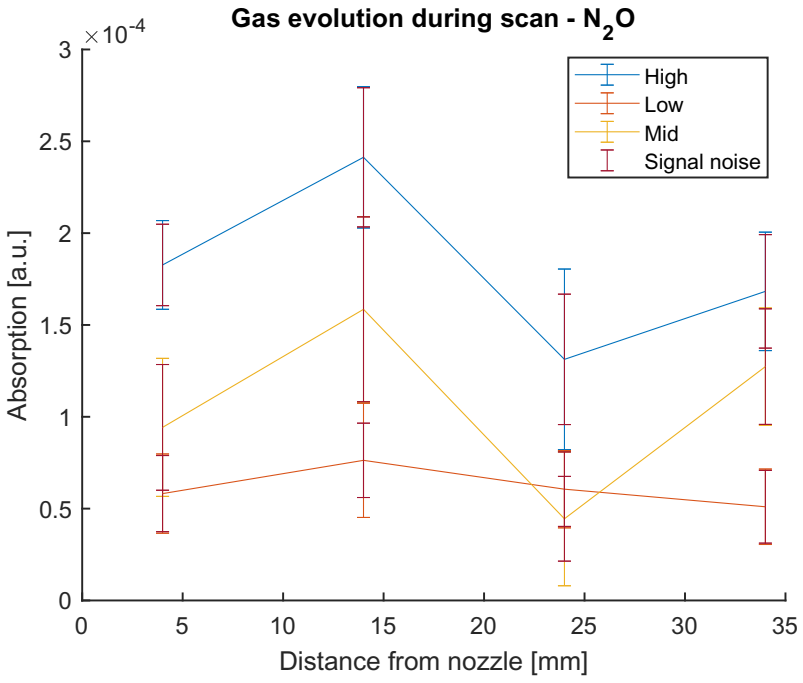

Figure 5.4: Estimated asymptotic value of the nitrous oxide concentration, in terms of integrated absorption, at different power configurations and as function of the distance from nozzle. Observe that the scale is an order of magnitude smaller than the ozone plot.

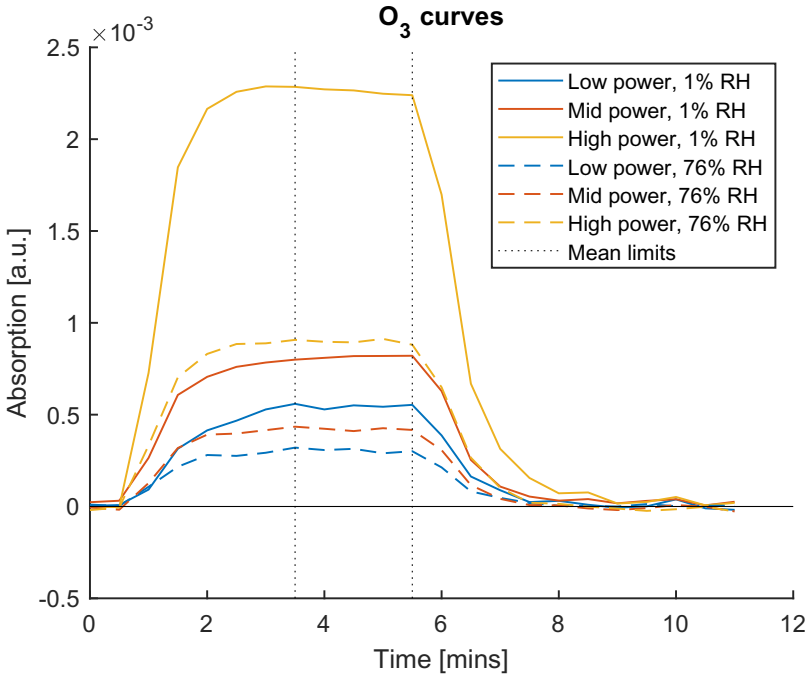

Figure 5.5: Integrated absorption of the ozone at different power configurations and humidities.

at maximum humidity and the ones at minimum one, for different power configurations. Data suggest that the higher the power, the more significant is the reduction of ozone production.

Power	RH≈ 1%	RH≈ 76%	Ratio
Low	$(5.5 \pm 0.1) \cdot 10^{-4}$	$(3.1 \pm 0.1) \cdot 10^{-4}$	0.56 ± 0.03
Mid	$(8.1 \pm 0.1) \cdot 10^{-4}$	$(4.2 \pm 0.1) \cdot 10^{-4}$	0.52 ± 0.01
High	$(22.6 \pm 0.2) \cdot 10^{-4}$	$(9.0 \pm 0.1) \cdot 10^{-4}$	0.397 ± 0.006

Table 5.1: Measured integrated absorptions and ratios.

This result, clear and with very small errors, has a great importance in the study of the PCC behavior. It suggests that the biological effects of the source can strongly vary in magnitude when the water presence in the interacting air changes. When biological studies are carried out, therefore, in quantifying the effects of the source one must keep track of the environmental humidity.

To understand the origin of this lowering, the decay of ozone after the PCC shutdown has been studied. Using an exponential decay function $y = Ae^{-t/\tau}$ the falling trend in fig. 5.5 is fitted and the obtained time constants are compared. Results are reported in fig. 5.7. Remembering that a point is acquired every 30s, and observing that the actual ozone decay last around 2min before the concentration fall below the noise level, it is clear that the significant points for the fits are about 5 for each decay curve: the estimation of τ results therefore to be affected by a large error. However, no strong trends are observed as function of humidity: this can suggest, even if very roughly, that there is not a trivial enhancement of ozone lysis reaction due to the presence of water.

Regarding other gases, the small sizes of the peaks does not allow carrying out precise analysis. For nitrous oxide the results are reported in figs. 5.8 and 5.9. As in the height scan, the signal is around one order of magnitude below the ozone one, and therefore the noise is way more significant; however, in this scan the results seems to be a bit more clean than the previous one and some deduction can be done. It can be clearly observed that in the high power configuration there is a larger production of the compound, but a clear trend is not visible. It must be pointed out that if there had been a trend as large as the ozone one, it would have been visible: the total compatibility

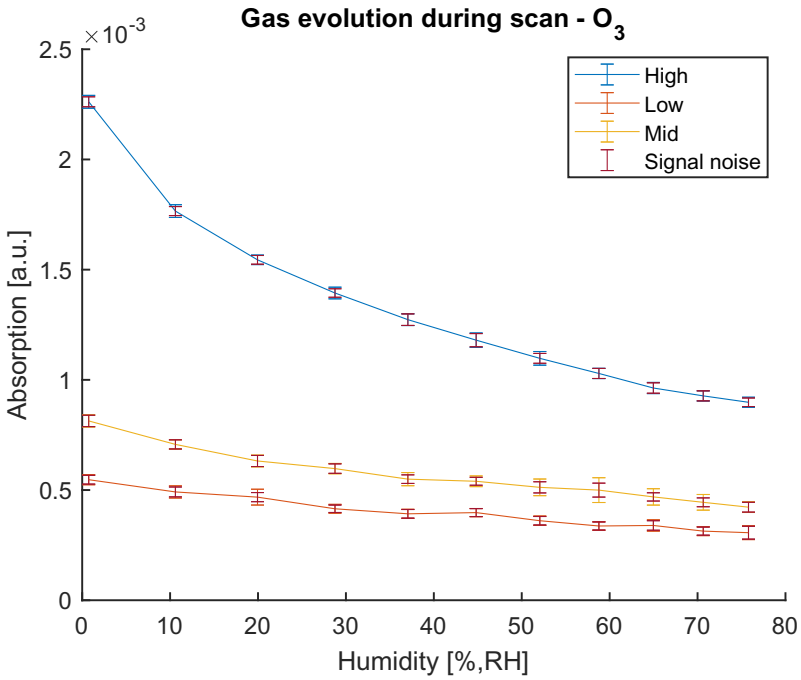

Figure 5.6: Estimated asymptotic value of the ozone concentration, in terms of integrated absorption, at different power configurations and as function of humidity.

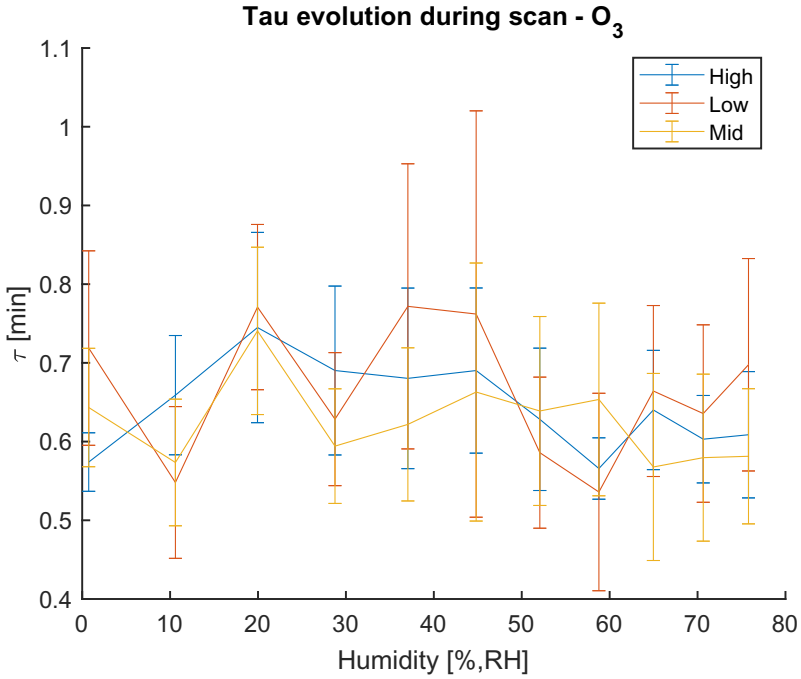

Figure 5.7: Time constants for O_3 decay tail, at different power configurations and as function of humidity.

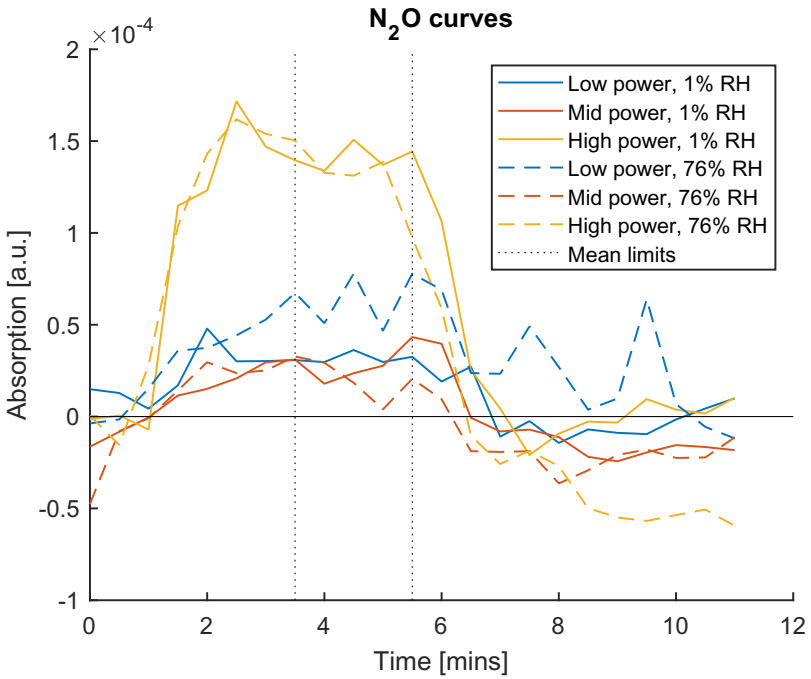

Figure 5.8: Integrated absorption of the nitrous oxide at different powers and humidities.

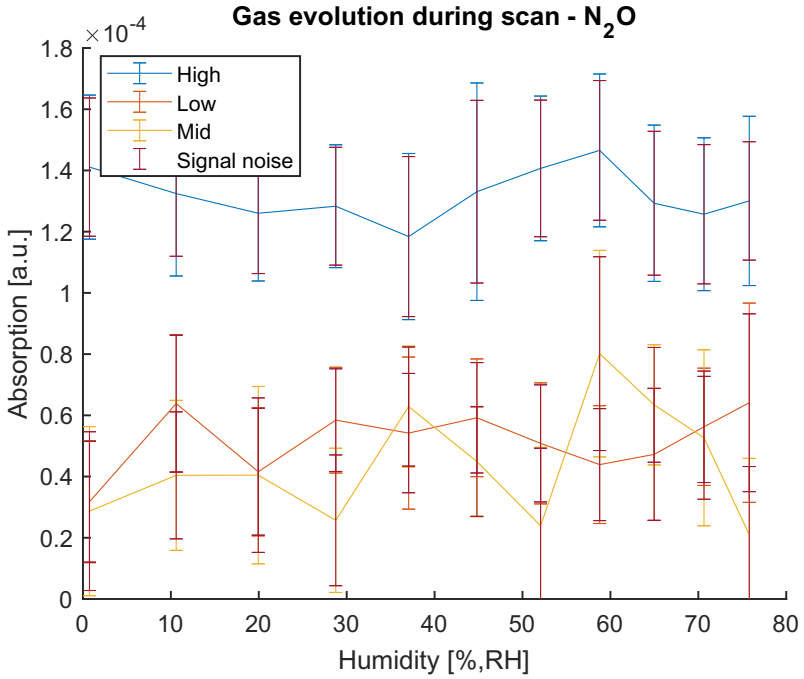

Figure 5.9: Estimated asymptotic value of the nitrous oxide concentration, in terms of integrated absorption, at different power configurations and as function of humidity.

of all the measurements suggest that there is no important variations on the concentration of this gas.

Also the other analyzed gases are very noisy and do not show significant trends.

5.4 Zero dimensional flows model

It is of particular interest the shape of the evolution curves in fig. 5.2 and 5.5. The phenomena affecting the quantity of ozone in the reactor are mainly two: production of ozone from the plasma plume and diffusion which lead the gas exiting the reactor. Let's, for simplicity, assume that there are not significant reactions of ozone lysis happening in the reactor.

Let's set up a zero dimensional model, which does not consider the ozone density profile inside the reactor itself but instead assume the reactor is in equilibrium at every moment. The assumption can be a bit strong in the growing and falling intervals but, having verified the good mixing of the gas in the chamber, it is quite safe in the stationary phase. The production of ozone can be described by a source term, S, which quantify the volume of ozone resulting from the plume; instead, the diffusion of ozone is given by the product between the total exiting flow P and the ozone volumetric fraction X. Let's assume, for simplicity, that both S and P are normalized to the total volume of the bioreactor: the resulting differential equation is

$$\frac{\partial X}{\partial t} = S - PX$$

The stationary phase is described by the condition:

$$\frac{\partial X}{\partial t} = 0 \quad \rightarrow \quad X = \frac{S}{P}$$

Observe that P is fixed to 3L/min (before normalization): assuming that pressure and temperature in the chamber are fixed at the atmospheric ones, the total outflow must match the total inflow. Also, S is certainly smaller than P, since the quantity of produced ozone cannot be higher than the total volume of injected gas: this means a suitable value of X that satisfies the equation always exists, regardless the actual value of S. The level of ozone, therefore, will always reach a stationary value after enough time of source activity.

Moreover, being P fixed, X and S are directly proportional: this confirms that, as assumed in the previous analysis, the stationary level reach by ozone concentration is indicative of the actual ozone production from the source.

The differential equation can also be directly solved obtaining the time evolution:

$$X(t) = \frac{S}{P} + \left(X_0 - \frac{S}{P}\right) e^{-Pt}$$

where X_0 is the initial ozone concentration. The two interesting behaviors are the rising curve, with $S \neq 0$ (the source is active) but $X_0 = 0$ (no ozone initially present), and the falling one, with $S = 0$ (the source is inactive) but $X_0 \neq 0$ (initial significant concentration of ozone):

$$X_{\text{rising}}(t) = \frac{S}{P}\left(1 - e^{-Pt}\right) \qquad X_{\text{falling}}(t) = X_0 e^{-Pt}$$

In both situations, an exponential behavior with time constant $\tau = \frac{1}{P}$ is expected: in particular, one can estimate:

$$\tau = \frac{1}{P} = \frac{V_{reactor}}{Q_{injected}} \approx \frac{1.7\text{L}}{3\text{L/min}} \approx 0.6\text{min}$$

The expected value is totally compatible with the one observed in the FTIR measurements; moreover, both the model and the observations agree in returning a τ independent of the power of the source, namely from the ozone production ratio. This firstly suggests that the diffusion of ozone inside the reactor itself is enough fast to not affect the rising and falling trends. Secondly, it is a strong hint that the main process responsible for ozone depletion is the gas outflow; no significant contribute from lysis reactions has been observed.

The exclusion of these effects leads to think that the variation in production of ozone observed with the variation of humidity in the environment should be ascribed to an efficiency difference in the ozone production chemical chains, and therefore in different rates of the synthesis reactions.

5.5 Chemical model for Ozone

In an article from Zhang et al. [Zha+16] the authors try to model the reactions which lead to ozone production during a dielectric barrier discharge. The modelled system is slightly different from the source here described, because helium is not present: they consider a discharge happening directly in air. However, from a qualitative point of view, given the fact that helium is essentially non-reacting the results can be considered valid even for the system considered in this work. The paper report a 0-dimensional (volume dynamic is not considered) simulation performed in a two stage model. A first phase, the *impulse stage*, is simulated for a short time and considers a bunch of free electrons introduced in the system and the electrons impact interactions, which lead to the creation of active species. In the second phase, named *relaxation stage*, instead, the interactions of active species with the surrounding gas are considered towards the reaching of a chemical equilibrium.

For the impulse stage, the environment is initially setup to contain only N_2, O_2 and H_2O, with the usual $1:4$ proportion between oxygen and nitrogen and a variable quantity of water vapor following the chosen RH. Moreover, a variable quantity of hot electrons in inserted. The reactions considered in this stage are:

$$O_2 + e \longrightarrow 2\,O + e \tag{RI1}$$
$$N_2 + e \longrightarrow 2\,N + e \tag{RI2}$$
$$H_2O + e \longrightarrow H + OH + e \tag{RI3}$$

and therefore O, N, H and OH are the only species, in addition to the initial ones, that can be present at the end of the first stage simulation.

For the relaxation stage, the initial environment corresponds to the final one of the impulse stage, but removing the electrons. In this stage a way larger set of reactions is considered (for the complete list, see the supplementary material of [Zha+16]). Among them, the most important one regarding the production of ozone is:

$$O + O_2 + M \longrightarrow O_3 + M \tag{RR1}$$

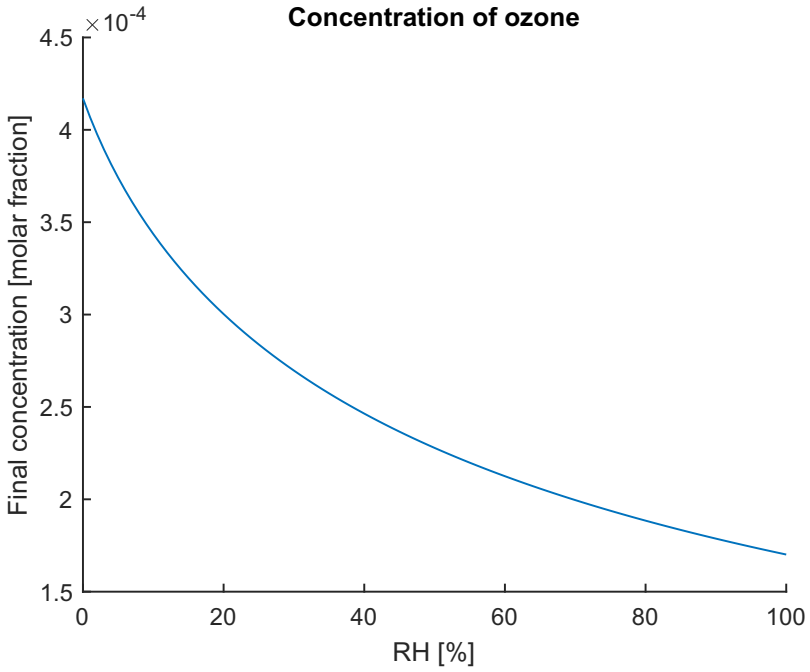

Figure 5.10: Concentrations of different gases, with initial electrons concentration 10^{-4}M and discharge time 1ns. Observe the significantly different scales for the two gases.

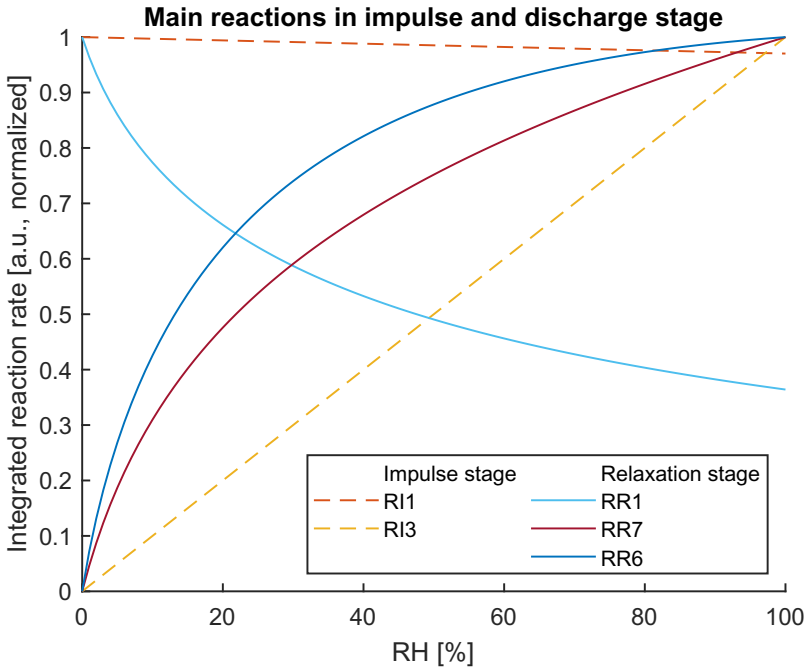

Figure 5.11: Integrated rates for various reactions, with initial electrons concentration 10^{-4}M and discharge time 1ns. The curves are individually normalized.

while the most important ones regarding its lysis are:

$$OH + O_3 \longrightarrow HO_2 + O_2 \quad \text{(RR2)}$$
$$HO_2 + O_3 \longrightarrow OH + 2\,O_2 \quad \text{(RR3)}$$
$$H + O_3 \longrightarrow OH + O_2 \quad \text{(RR4)}$$
$$H + O_3 \longrightarrow HO_2 + O \quad \text{(RR5)}$$

Another couple of reactions must be mentioned:

$$HO_2 + O \longrightarrow OH + O_2 \quad \text{(RR6)}$$
$$O + OH \longrightarrow O_2 + H \quad \text{(RR7)}$$

which are the main competitors of reaction RR1 in the consumption of atomic oxygen.

The behavior of the chemical simulation is controlled by two parameters: the duration of the impulse stage and the initial concentration of electrons. Both the values are unknown for the PCC system, which means a precise simulation cannot be carried out. In fact, one must observe that when modelling the PCC source the impulse stage does not simply correspond to the discharge: a more precise simulation should consider the dynamic of the bullets exiting the nozzle and ionizing the atmosphere and the electrons avalanches which are created.

However, the simulation has been repeated using the same protocol and the same routines suggested by Zhang, and varying the control parameters in the plausibility range.

The results obtained for ozone (an example of which is reported in fig. 5.10) appears to be qualitatively independent of the two control parameters. The trend obtained is similar to the one previously measured: the production of ozone in the simulations is reduced when more humid air is considered. The simulations, moreover, allow to obtain the reactions rates (see, for example, fig. 5.11), again returning at least for ozone behaviors qualitatively independent of the control parameters. As stated in the paper and confirmed by the repeated simulations, in dry air the production of ozone is straight forward and proportional to the initial quantity of O_2 available: reactions RI1 and RR1 results in a direct path from excited electrons to ozone. When water is present, instead, reaction RI1 is reduced in favor of reaction RI3, resulting in a lower availability

of atomic oxygen and in a higher presence of H and OH. Moreover, these last two active species enhances the reactions RR6 and RR7, which consume the available atomic oxygen reducing the rate of reaction RR1. Finally, as previously found in both measurements and in the flows model, reactions RR2-RR5 turn out to have negligible rates and therefore a not significant role in the determination of final gases concentrations.

Again, this analysis and the simulation agree in stating that the reduction of the presence of ozone is not due to an enhancement of the lysis reactions but to a reduction of the synthesis ones, given by the emergence of competitive paths involving water which lead to the production of hydrogen and hydroxy radicals.

Regarding the production of nitrous oxide, instead, the results of the simulation are more complex and way more dependent from the two control parameters: the expected trend varies from rising to falling, and therefore no useful suggestions can be obtained.

Conclusions

This thesis work focuses on the analysis of the production of reactive oxygen and nitrogen species in the Plasma Coagulation Controller, a cold atmospheric plasma source developed in Padova laboratories with wound healing and disinfection purposes. The chosen diagnostic is the Fourier-transform infrared spectroscopy, which has been proven to be a very powerful diagnostic, allowing to detect numerous chemical species even if their concentrations are low. On the other hand, the dimension of the plasma plume in the Plasma Coagulation Controller is very small, and the quantity of produced reactive species is hard to detect.

During the thesis work, a fully operative system for adapting the PCC to the FTIR has been set up. The electrical behavior of the source has been firstly studied, characterizing the electrical impulses corresponding to the three power configurations (low, middle and high); then, a rough tests on *Escherichia coli* confirmed the bactericidal effects previously studied. Controls on gases flows have been carried out observing the behavior of the plume in saturated helium conditions: the disappearing of the plume with the exhaustion of air availability has been noticed, confirming the fundamental role of the mixing layer in the propagation of plasma bullets. Temperature controls, finally, confirmed the coldness of the produced plasma, which guarantees the absence of thermal stress on the treated substrates.

A wide work on reducing all the possible errors and noise sources has been carried out, both regarding hardware and software improvements. Recognized the noisy character of the baseline shifting and tilting, its origin has been searched and found in the reactor windows, which has been replaced; then, the system for the production and injection of humid air has been tested and characterized. Finally, an automatic script for the correction of the baseline tilting and the cleaning of the water peaks has been developed.

In the end, a satisfying quality for the signal has been reached. This allows to recognize the production of ozone, nitrous oxide and nitric acid, confirming the theories about the production of RONS in the source.

After defining an estimator for the size of the peaks and a protocol for the acquisition of data, scans has been carried out varying the power coupled to the plasma plume, the distance of the infrared beam from the nozzle and the humidity in the environment. The production of ozone has been proven to be sensitive to the power regime, rising when passing from low to middle and to high power; with respect to its dependence from the distance from the nozzle, instead, no significant variations have been measured. A strong dependence on the production of ozone with respect to the humidity has been observed: as the humidity rises, in fact, the production of ozone has been proven to significantly fall. Searching for the origins of this falling, a flows model and a chemical one have been proposed. The predictions from both models turn out to be fully compatible with the measurements: the ozone production variation has been recognized to be ascribable to a reduction of ozone synthesis reactions in favor of hydrogen and hydroxy radicals production.

For other gases, the available setup does not allow observing variations in productions, given the small quantities involved.

The results obtained leave space for further work in multiple directions. Firstly, the setup can be improved even more, possibly redesigning the bioreactor to a smaller volume to avoid species dispersion; this can allow to study the behaviors of different species other than ozone as functions of environmental conditions. Secondly, proven the sensitivity of RONS production to the humidity of atmosphere, the biological tests can be repeated in humidity-controlled setups, correlating the coagulation efficiency and the disinfection one with the production of reactive species: this can give suggestions on the real actors involved in biological processes. Moreover, a combined study

can be done, measuring the quantity of RONS when the plasma source reacts with a substrate, for example blood: absorption or releasing of particular species can give hints on the activated coagulation chain. Even different kinds of diagnostics can be exploited, to observe other regions of spectra: for example, with visible-UV spectrophotometry the presence of OH can be detected. It can be interesting, given the prediction of the chemical model for a rising of OH with the falling of O_3, to compare humidity measurements with the two instruments. Finally, the same measurements can be carried out with different kind of sources: systems driven by a regular MHz sinusoidal high voltage are known to have a different behavior with respect to pulsed ones, and the production of RONS can be studied in a standardized apparatus.

The method and the results exposed in this work can be useful for a systematic and standardized study on the production of RONS in plasma jet for medical applications. After an upgrade of the system to enhance both sensitivity and flexibility, using protocols similar to the here tested ones, a measurement of different sources in different power regimes can be carried out comparing the efficiencies in terms of RONS production.

Bibliography

[Bek+19] Sander Bekeschus, Pietro Favia, Eric Robert, and Thomas von Woedtke. "White Paper on Plasma for Medicine and Hygiene: Future in Plasma Health Sciences". In: *Plasma Processes and Polymers* 16.1 (2019). ISSN: 1612-8869. DOI: 10.1002/ppap.201800033.

[BH09] Catherine Berthomieu and Rainer Hienerwadel. "Fourier Transform Infrared (FTIR) Spectroscopy". In: *Photosynthesis Research* 101.2-3 (Sept. 2009), pp. 157–170. ISSN: 0166-8595, 1573-5079. DOI: 10.1007/s11120-009-9439-x.

[BH14] Mitra Bahri and Fariborz Haghighat. "Plasma-Based Indoor Air Cleaning Technologies: The State of the Art-Review". In: *CLEAN – Soil, Air, Water* 42.12 (2014), pp. 1667–1680. ISSN: 1863-0669. DOI: 10.1002/clen.201300296.

[BJ11] Graham J. Burton and Eric Jauniaux. "Oxidative Stress". In: *Best Practice & Research Clinical Obstetrics & Gynaecology* 25.3 (June 2011), pp. 287–299. ISSN: 15216934. DOI: 10.1016/j.bpobgyn.2010.10.016.

[BMR12] D Breden, K Miki, and L L Raja. "Self-Consistent Two-Dimensional Modeling of Cold Atmospheric-Pressure Plasma Jets/Bullets". In: *Plasma Sources Science and Technology* 21.3 (June 1, 2012), p. 034011. ISSN: 0963-0252, 1361-6595. DOI: 10.1088/0963-0252/21/3/034011.

[Bru] Bruker. *Bruker Vertex 80v Brochure and Specifications*.

[Cor+19a] Luigi Cordaro et al. "On the Electrical and Optical Features of the Plasma Coagulation Controller Low Temperature Atmospheric Plasma Jet". In: *Plasma* 2.2 (2 June 2019), pp. 156–167. DOI: 10.3390/plasma2020012.

[Cor+19b] Luigi Cordaro et al. "The Role of Thermal Effects in Plasma Medical Applications: Biological and Calorimetric Analysis". In: *Applied Sciences* 9.24 (Dec. 17, 2019). ISSN: 2076-3417. DOI: 10.3390/app9245560.

[Dai+18] Xiaofeng Dai, Kateryna Bazaka, Derek J. Richard, Erik (Rik) W. Thompson, and Kostya (Ken) Ostrikov. "The Emerging Role of Gas Plasma in Oncotherapy". In: *Trends in Biotechnology* 36.11 (Nov. 2018), pp. 1183–1198. ISSN: 01677799. DOI: 10.1016/j.tibtech.2018.06.010.

[De +18] Gianluca De Masi et al. "Plasma Coagulation Controller: A Low- Power Atmospheric Plasma Source for Accelerated Blood Coagulation". In: *Plasma Medicine* 8.3 (2018). ISSN: 1947-5764, 1947-5772. DOI: 10.1615/PlasmaMed.2018028202.

[Gra12] David B. Graves. "The Emerging Role of Reactive Oxygen and Nitrogen Species in Redox Biology and Some Implications for Plasma Applications to Medicine and Biology". In: *Journal of Physics D: Applied Physics* 45.26 (June 2012), p. 263001. ISSN: 0022-3727. DOI: 10.1088/0022-3727/45/26/263001.

[Gra14] David B Graves. "Low Temperature Plasma Biomedicine: A Tutorial Review". In: *Phys. Plasmas* (2014), p. 13.

[GTC18] Matteo Gherardi, Riccardo Tonini, and Vittorio Colombo. "Plasma in Dentistry: Brief History and Current Status". In: *Trends in Biotechnology* 36.6 (June 2018), pp. 583–585. ISSN: 01677799. DOI: 10.1016/j.tibtech.2017.06.009.

[Hae+14] Beate Haertel, Thomas von Woedtke, Klaus-Dieter Weltmann, and Ulrike Lindequist. "Non-Thermal Atmospheric-Pressure Plasma Possible Application in Wound Healing". In: *Biomolecules & Therapeutics* 22.6 (Nov. 2014), pp. 477–490. ISSN: 1976-9148. DOI: 10.4062/biomolther.2014.105. pmid: 25489414.

[HG07] Werner Herres and Joern Gronholz. *Understanding FT-IR Data Processing.* 2007.

[Ike+15] Sanae Ikehara et al. "Plasma Blood Coagulation Without Involving the Activation of Platelets and Coagulation Factors". In: *Plasma Processes and Polymers* 12.12 (2015), pp. 1348–1353. ISSN: 1612-8869. DOI: 10.1002/ppap.201500132.

[JLK10] Julien Jarrige, Mounir Laroussi, and Erdinc Karakas. "Formation and Dynamics of Plasma Bullets in a Non-Thermal Plasma Jet: Influence of the High-Voltage Parameters on the Plume Characteristics". In: *Plasma Sources Science and Technology* 19.6 (Dec. 1, 2010), p. 065005. ISSN: 0963-0252, 1361-6595. DOI: 10.1088/0963-0252/19/6/065005.

[Kal+07] Sameer U. Kalghatgi et al. "Mechanism of Blood Coagulation by Nonthermal Atmospheric Pressure Dielectric Barrier Discharge Plasma". In: *IEEE Transactions on Plasma Science* 35.5 (Oct. 2007), pp. 1559–1566. ISSN: 1939-9375. DOI: 10.1109/TPS.2007.905953.

[Kei18] Michael Keidar. "A Prospectus on Innovations in the Plasma Treatment of Cancer". In: *Physics of Plasmas* 25.8 (Aug. 2018), p. 083504. ISSN: 1070-664X, 1089-7674. DOI: 10.1063/1.5034355.

[Kon+09] M. G. Kong et al. "Plasma Medicine: An Introductory Review". In: *New Journal of Physics* 11.11 (Nov. 2009). ISSN: 1367-2630. DOI: 10.1088/1367-2630/11/11/115012.

[Lar18] Mounir Laroussi. "Effects of Low Temperature Plasmas on Proteins". In: *IEEE Transactions on Radiation and Plasma Medical Sciences* 2.3 (May 2018), pp. 229–234. ISSN: 2469-7303. DOI: 10.1109/TRPMS.2018.2796308.

[Lar20] Mounir Laroussi. "Cold Plasma in Medicine and Healthcare: The New Frontier in Low Temperature Plasma Applications". In: *Frontiers in Physics* 8 (2020). ISSN: 2296-424X. DOI: 10.3389/fphy.2020.00074.

[Lar96] M. Laroussi. "Sterilization of Contaminated Matter with an Atmospheric Pressure Plasma". In: *IEEE Transactions on Plasma Science* 24.3 (June 1996), pp. 1188–1191. ISSN: 1939-9375. DOI: 10.1109/27.533129.

[Man19] Davide Mancini. "Development and Characterization of an Atmospheric Plasma Source for Non-Thermal Blood Coagulation". Università degli Studi di Padova, 2019. 103 pp.

[Nat] National Institute of Standards and Technology. *Chemistry WebBook (Standard Reference Database 69).* DOI: 10.18434/T4D303.

[The] Thermo Scientific. *Introduction to Fourier Transform Infrared Spectroscopy.*

[vWoe+13] Th. von Woedtke, S. Reuter, K. Masur, and K.-D. Weltmann. "Plasmas for Medicine". In: *Physics Reports* 530 (Sept. 1, 2013), pp. 291–320. ISSN: 0370-1573. DOI: 10.1016/j.physrep.2013.05.005.

[Yan+20] Dayun Yan et al. "A Physically Triggered Cell Death via Transbarrier Cold Atmospheric Plasma Cancer Treatment". In: *ACS Applied Materials & Interfaces* 12.31 (Aug. 5, 2020), pp. 34548–34563. ISSN: 1944-8244. DOI: 10.1021/acsami.0c06500.

[Zha+16] Xuming Zhang, Bok Jik Lee, Hong G. Im, and Min Suk Cha. "Ozone Production With Dielectric Barrier Discharge: Effects of Power Source and Humidity". In: *IEEE Transactions on Plasma Science* 44.10 (Oct. 2016), pp. 2288–2296. ISSN: 0093-3813, 1939-9375. DOI: 10.1109/TPS.2016.2601246.